The Astrophysical Journal, 954:55 (16pp), 2023 September 1 https://doi.org/10.3847/1538-4357/ace3c1


# Abundance Analysis of Stars at Large Radius in the Sextans Dwarf Spheroidal Galaxy*

Ian U. Roederer[1,2], Andrew B. Pace[3], Vinicius M. Placco[4], Nelson Caldwell[5], Sergey E. Koposov[6,7,8], Mario Mateo[1], Edward W. Olszewski[9], and Matthew G. Walker[3]
[1] Department of Astronomy, University of Michigan, Ann Arbor, MI 48109, USA; iur@umich.edu
[2] Joint Institute for Nuclear Astrophysics—Center for the Evolution of the Elements (JINA-CEE), East Lansing, MI 48824, USA
[3] McWilliams Center for Cosmology, Carnegie Mellon University, Pittsburgh, PA 15213, USA
[4] NSF's NOIRLab, Tucson, AZ 85719, USA
[5] Harvard-Smithsonian Center for Astrophysics, Cambridge, MA 02138, USA
[6] Institute for Astronomy, University of Edinburgh, Royal Observatory, Edinburgh, EH9 3HJ, UK
[7] Institute of Astronomy, University of Cambridge, Cambridge, CB3 0HA, UK
[8] Kavli Institute for Cosmology, University of Cambridge, Cambridge, CB3 0HA, UK
[9] The University of Arizona, Steward Observatory, 933 North Cherry Avenue, Tucson, AZ 85721, USA
*Received 2023 June 1; revised 2023 June 29; accepted 2023 June 30; published 2023 August 22*

## Abstract

We present the stellar parameters and chemical abundances of 30 elements for five stars located at large radii (3.5–10.7 times the half-light radius) in the Sextans dwarf spheroidal galaxy. We selected these stars using proper motions, radial velocities, and metallicities, and we confirm them as metal-poor members of Sextans with $-3.34 \leqslant$ [Fe/H] $\leqslant -2.64$ using high-resolution optical spectra collected with the Magellan Inamori Kyocera Echelle spectrograph. Four of the five stars exhibit normal abundances of C ($-0.34 \leqslant$ [C/Fe] $\leqslant +0.36$), mild enhancement of the $\alpha$ elements Mg, Si, Ca, and Ti ([$\alpha$/Fe] $= +0.12 \pm 0.03$), and unremarkable abundances of Na, Al, K, Sc, V, Cr, Mn, Co, Ni, and Zn. We identify three chemical signatures previously unknown among stars in Sextans. One star exhibits large overabundances ([X/Fe] $> +1.2$) of C, N, O, Na, Mg, Si, and K, and large deficiencies of heavy elements ([Sr/Fe] $= -2.37 \pm 0.25$, [Ba/Fe] $= -1.45 \pm 0.20$, [Eu/Fe] $< +0.05$), establishing it as a member of the class of carbon-enhanced metal-poor stars with no enhancement of neutron-capture elements. Three stars exhibit moderate enhancements of Eu ($+0.17 \leqslant$ [Eu/Fe] $\leqslant +0.70$), and the abundance ratios among 12 neutron-capture elements are indicative of *r*-process nucleosynthesis. Another star is highly enhanced in Sr relative to heavier elements ([Sr/Ba] $= +1.21 \pm 0.25$). These chemical signatures can all be attributed to massive, low-metallicity stars or their end states. Our results, the first for stars at large radius in Sextans, demonstrate that these stars were formed in chemically inhomogeneous regions, such as those found in ultra-faint dwarf galaxies.

*Unified Astronomy Thesaurus concepts:* Dwarf spheroidal galaxies (420); Nucleosynthesis (1131); Stellar abundances (1577)

*Supporting material:* machine-readable table

## 1. Introduction

The chemical compositions of old stars reflect which elements were produced, and in what amounts, by the earliest generations of stars and supernovae. Old stars are found in many Galactic environments, including the surviving populations of dwarf galaxies surrounding the Milky Way. The star formation histories of the lowest mass dwarf galaxies, often referred to as ultra-faint dwarf (UFD) galaxies indicate that these systems formed large fractions—up to ≈80%—of their stars before the end of reionization (Brown et al. 2014). Stellar chemistry supports this conclusion. Detailed chemical analysis of individual stars in UFD galaxies reveals that they host relatively high fractions of stars that may have formed from the remnants of zero-metallicity Population III stars (Frebel & Norris 2015, and references therein).

More massive dwarf galaxies, often referred to as classical dwarf spheroidal (dSph) galaxies, also formed relatively high fractions of their stars at early times (e.g., Revaz et al. 2009; Weisz et al. 2014). The dSph galaxies are massive enough to have sustained internal chemical evolution, so chemical signatures associated with the earliest stars and supernovae are rare (e.g., Starkenburg et al. 2010; Kirby et al. 2011b), but present (e.g., Fulbright et al. 2004; Frebel et al. 2010; Skúladóttir et al. 2023).

Most previous studies have focused on stars in the central regions of dSph galaxies, but recent efforts have confirmed members at large separations from their centers. These efforts have been based on spectroscopic follow-up of wide-field photometric searches (e.g., Muñoz et al. 2005, 2006; Westfall et al. 2006; Hendricks et al. 2014) or wide-field broadband photometry combined with proper-motion measurements from the Gaia mission (Prusti et al. 2016). Studies by Chiti et al. (2021, 2023), Filion & Wyse (2021), Longeard et al. (2022, 2023), Qi et al. (2022), Yang et al. (2022), and Sestito et al. (2023a, 2023b) have shown that several dSph and UFD galaxies contain stars near their tidal radii. These extended stellar halos may have formed through dwarf galaxy mergers

* This paper includes data gathered at the 6.5 m Magellan Telescopes located at Las Campanas Observatory, Chile. Other observations reported here were obtained at the MMT Observatory, a joint facility of the Smithsonian Institution and the University of Arizona. This paper is also based on archival observations collected at the European Southern Observatory under ESO program(s) 0102.B-0786(C).

(Rey et al. 2019; Tarumi et al. 2021), and multiple mergers may have occurred within individual dSph galaxies around the Milky Way (Griffen et al. 2018; Deason et al. 2023). These stars frequently exhibit low metallicities, [Fe/H] $< -2$. The outer regions of UFD and dSph galaxies may host previously unrecognized reservoirs of stars whose chemical enrichment was potentially dominated by the earliest generations of stars and supernovae.

Our study builds on previous work by examining the chemistry of stars in the outer regions of the Sextans dSph galaxy for the first time.Sextans is 89 kpc from the center of the Milky Way (Fritz et al. 2018). Battaglia et al. (2022) computed orbit integrations for Sextans that account for the reflex motion of the Large Magellanic Cloud on the Milky Way. These calculations indicate that Sextans is on a moderately eccentric orbit ($e \approx 0.28$), with an orbital pericenter around 72 kpc and an orbital apocenter around 129 kpc. The period of star formation in Sextans was mainly limited to ≈0.8 Gyr (Kirby et al. 2011a) within the first ≈1.3 Gyr after the Big Bang (Bettinelli et al. 2018).

Sextans exhibits evidence for internal stellar substructure. Kleyna et al. (2004) and Walker et al. (2006) identified possible dynamically cold substructure near the core of Sextans. Battaglia et al. (2011) found evidence for two chemodynamical stellar populations in Sextans. Roderick et al. (2016) found evidence of an extended, gravitationally bound stellar structure within the tidal radius. This stellar substructure is probably unrelated to disruptive tidal effects, as Cicuéndez et al. (2018) found no significant distortions or signs of tidal disturbances in Sextans. The stellar substructure could be related to accretion. Cicuéndez & Battaglia (2018) identified a ring-like structure surrounding the inner regions (≈15′–20′) of Sextans. This feature is characterized by a small velocity offset and lower metallicity relative to the surrounding stellar fields (Walker et al. 2009a). Finally, Kim et al. (2019) identified a metal-poor stellar overdensity in Sextans that might be a low-mass star cluster undergoing dissolution.Sextans is not unusual among dSph galaxies in exhibiting substructure (e.g., Olszewski & Aaronson 1985; Battaglia et al. 2006; Olszewski et al. 2006; Amorisco et al. 2014; Pace et al. 2020).

Previous studies have derived detailed chemical abundances of stars in Sextans using high-resolution spectroscopy (Shetrone et al. 2001; Aoki et al. 2009; Tafelmeyer et al. 2010; Honda et al. 2011; Aoki et al. 2020; Lucchesi et al. 2020; Theler et al. 2020; Mashonkina et al. 2022; Fernandes et al. 2023). These studies have been limited to stars near the center of Sextans, within the inner ≈40′ or so. They have found chemical abundance behaviors that are relatively typical for dSph galaxies. These signatures include enhanced abundances of $\alpha$ elements (where $\alpha$ represents O, Mg, Si, Ca, and Ti) in the lowest metallicity stars ([Fe/H] $< -2.8$ in Sextans). This behavior indicates that core-collapse supernovae dominated the chemical enrichment at early times when the most metal-poor stars likely were forming. The [$\alpha$/Fe] ratios exhibit a so-called *knee* when plotted against [Fe/H], either at [Fe/H] $\approx -2.5$ or $-2.0$. Stars with metallicities higher than this knee exhibit lower [$\alpha$/Fe] ratios, a behavior typically explained by contributions from Type Ia supernovae. Two knees could indicate the presence of slightly older and slightly younger populations of stars, which could be a potential accretion signature (Benítez-Llambay et al. 2016; Reichert et al. 2020; Mashonkina et al. 2022). The most metal-poor stars in Sextans exhibit subsolar [Sr/Fe] and [Ba/Fe] ratios, which might signal the presence of small amounts of material produced by the weak component of the rapid neutron-capture process (*r*-process). Some metal-rich ([Fe/H] $> -2.2$) stars in Sextans exhibit signatures of the slow neutron-capture process (*s*-process), which appears on delayed timescales and occurs in low- or intermediate-mass stars that pass through the asymptotic giant branch (AGB) phase of evolution. Few carbon-enhanced stars are known in Sextans (Honda et al. 2011; Theler et al. 2020; Mashonkina et al. 2022).

We report on the chemical abundances of five stars at large radius in Sextans. These stars exhibit abundance patterns previously unrecognized in Sextans, including large enhancements of carbon and other light elements, and several distinct signatures among the heaviest elements. Our manuscript is structured as follows. Section 2 presents our target selection and new spectroscopic data. Section 3 describes our abundance analysis of these spectra. Section 4 presents our results and compares them with previous work. Section 5 discusses these results, and Section 6 summarizes our conclusions.

## 2. Data

### 2.1. Target Selection

Our targets were selected as confirmed members in radial velocity surveys (A. B. Pace et al. 2023, in preparation) or from a proper-motion-based selection (Pace et al. 2022) using Gaia's Early Data Release 3 (EDR3; Brown et al. 2021). We focused on bright ($G \lesssim 17.5$) and distant ($R_e/R_h \gtrsim 3$) stars, where $G$ is the Gaia broadband photometric magnitude, $R_e \equiv \sqrt{x^2 + y^2/q^2}$ is the deprojected elliptical radius, and $R_h$ is the Sextans half-light radius (16.′9 ± 0.′1; Muñoz et al. 2018). We identified J1015-0238 as a radial velocity member from spectra collected using the Hectochelle spectrograph (Szentgyorgyi et al. 2011) at the MMT Observatory. We identified J1018-0209 and J1008+0001 from archival spectra collected using the Fiber Large Array Multi Element Spectrograph's GIRAFFE instrument (Pasquini et al. 2002) at the Very Large Telescope. Other targets lack previous radial velocity measurements, so we considered their membership probabilities from Pace et al. and examined photometry from the ninth data release of the Dark Energy Camera Legacy Survey (DECaLS DR9; Dey et al. 2019). We compared the locations of candidate members and spectroscopic members in $g - r$ versus $g$ color–magnitude diagrams and $g - r$ versus $r - z$ color–color diagrams. We obtained low signal-to-noise (S/N) spectra (Section 2.2) to measure radial velocities to confirm membership before obtaining longer observations with higher S/N ratios. Table 1 lists the target names, coordinates, the ratio of $R_e$ to $R_h$, selected photometry, and reddening estimates for the stars in our sample.

Figure 1 illustrates the spatial distribution of the stars in our sample and previous high-resolution and medium-resolution spectroscopic samples. The stars in our high-S/N sample (Section 2.2), shown by the orange stars, span $3.5 < R_e/R_h < 10.7$. These stars are located at much larger radii than previous high-resolution samples, which are concentrated within 4 $R_e/R_h$, and the vast majority of which are within 2 $R_e/R_h$. The King tidal (or limiting) radius, $R_t$, is uncertain for Sextans, with estimates of 3.7 $R_h$ (Muñoz et al. 2018), 5.0 $R_h$ (Roderick et al. 2016), and 6.2 $R_h$ (Tokiwa et al. 2023). At least two, and possibly four, of the five stars in our high-S/N sample are beyond $R_t$, which is roughly the radius at

**Table 1**
Star Names, Coordinates, Photometry, and Reddening

| Source_ID (Gaia[a]) | Star Name (SDSS[b]) | Star Name (Adopted) | R.A. (J2000) | Decl. (J2000) | $R_e/R_h$ | $G$ (Gaia) | $g$ (SDSS) | $B$ ([c]) | $V$ ([c]) | $E(B-V)$ (SF11[d]) | $E(B-V)$ (Na I) | $E(B-V)$ (Adopted) |
|---|---|---|---|---|---|---|---|---|---|---|---|---|
| Stars with high-S/N observations | | | | | | | | | | | | |
| 3831812247731524608 | J100801.54+000108.1 | J1008+0001 | 10:08:01.54 | +00:01:08.1 | 10.68 | 18.49 | 18.80 | 19.38 | 18.27 | 0.027 | 0.012 | 0.02 |
| 3828963348679468032 | J101039.85-022007.8 | J1010-0220 | 10:10:39.85 | −02:20:07.8 | 3.56 | 17.23 | 18.12 | 18.68 | 17.63 | 0.034 | >0.044 | 0.04 |
| 3828784987277714560 | J101542.20-023838.6 | J1015-0238 | 10:15:42.21 | −02:38:38.7 | 6.36 | 17.08 | 18.01 | 18.58 | 17.50 | 0.031 | 0.021 | 0.03 |
| 3830390720930784640 | J101800.19-015521.4 | J1018-0155 | 10:18:00.20 | −01:55:21.5 | 5.79 | 16.98 | 18.03 | 18.63 | 17.47 | 0.043 | >0.066 | 0.05 |
| 3830319390113933952 | J101837.07-020936.2 | J1018-0209 | 10:18:37.08 | −02:09:36.3 | 7.06 | 17.55 | 17.91 | 18.52 | 17.33 | 0.038 | >0.031 | 0.04 |
| Stars with low-S/N observations | | | | | | | | | | | | |
| 3829054779943345536 | J101341.76-021124.4 | J1013-0211 | 10:13:41.76 | −02:11:24.4 | 3.04 | 16.75 | 17.86 | 18.48 | 17.27 | 0.033 | ⋯ | ⋯ |
| 3830721875794075904 | J101435.84-005401.4 | J1014-0054 | 10:14:35.84 | −00:54:01.4 | 3.28 | 16.84 | 17.95 | 18.58 | 17.34 | 0.034 | ⋯ | ⋯ |

**Notes.**
[a] Gaia EDR3 (Brown et al. 2021).
[b] Sloan Digital Sky Survey Data Release 13 (SDSS DR13; Albareti et al. 2017.)
[c] The $B$ and $V$ magnitudes are calculated from the SDSS $g$ magnitude using the Population II star transformations of Jordi et al. (2006).
[d] Schlafly & Finkbeiner (2011).

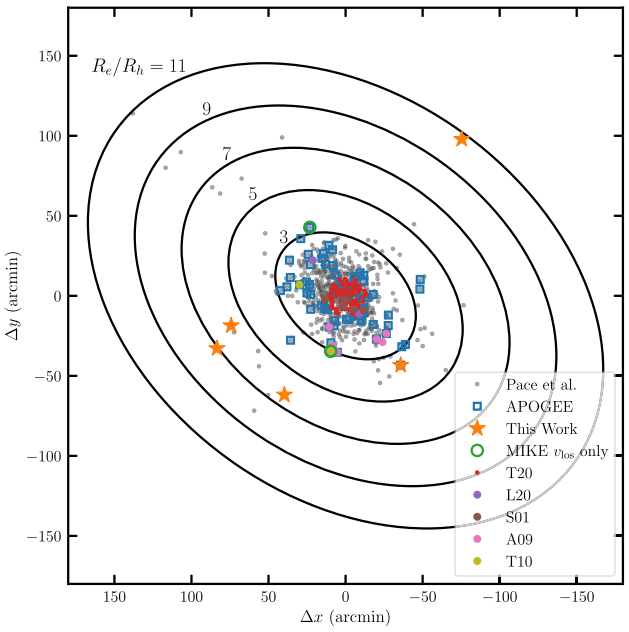


**Figure 1.** Plot of the spatial distribution of our sample (orange stars and green circles) and previous spectroscopic samples of stars in Sextans: T20 = Theler et al. (2020), L20 = Lucchesi et al. (2020), S01 = Shetrone et al. (2001), A09 = Aoki et al. (2009), and T10 = Tafelmeyer et al. (2010). The small gray dots mark stars observed in our medium-resolution work (Pace et al. 2023, in preparation). The ellipses indicate multiples of $R_h$.

which the stellar overdensity of the dwarf galaxy falls below that of the Milky Way foreground.

Figure 2 illustrates the line-of-sight velocity, $v_{los}$, as a function of radial distance from the center of the Sextans dSph. Our $v_{los}$ measurements agree with previous values, when available, and they cluster around the systemic $v_{los}$ of the Sextans dSph, $224.3 \pm 0.1$ km s$^{-1}$ (Walker et al. 2009b). The stars in our sample are high-probability members of Sextans.

### 2.2. Observations

We used the Magellan Inamori Kyocera Echelle (MIKE; Bernstein et al. 2003) spectrograph on the Landon Clay (Magellan II) Telescope at Las Campanas Observatory, Chile, to collect high-resolution spectra of seven stars in Sextans. These spectra were obtained on several nights in 2021 and 2022 during dark time and under excellent seeing conditions (≈0.″4–0.″8). The $0.''7 \times 5.''0$ entrance slit and $2 \times 2$ binning on the CCD yield a spectral resolving power of $R \equiv \lambda/\Delta\lambda \sim 41,000$ on the blue spectrograph (3350 $< \lambda <$ 5000 Å) and $R \sim 36,000$ on the red spectrograph (5000 $< \lambda <$ 9150 Å). We observed each star using a series of exposures, ranging from 1500–2300 s each. We obtained ThAr comparison spectra immediately before or after the series of exposures of each star. Table 2 summarizes the observing date, UT at mid-observation, total exposure time, heliocentric $v_{los}$, and S/N ratios at several wavelengths in the co-added spectrum of each star. We focus our attention on the five stars with high S/N ratios.

We use the CarPy MIKE reduction pipeline (Kelson et al. 2000; Kelson 2003) to perform the overscan subtraction, pixel-to-pixel flat field division, image coaddition, cosmic ray removal, sky and scattered-light subtraction, rectification of the tilted slit profiles along the orders, spectrum extraction, and wavelength calibration. We use the IRAF (Tody 1993) software package to stitch together and continuum normalize the spectra.

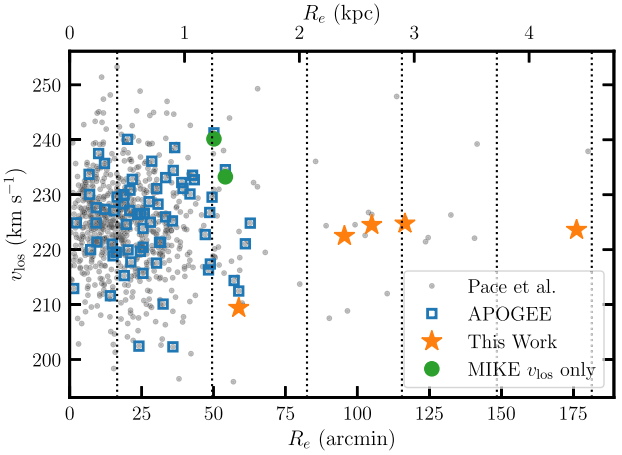


**Figure 2.** Comparison of $R_e$ vs. $v_{los}$ for stars in Sextans. The scale on the top axis assumes a distance of 86.1 kpc (Helmi et al. 2018). Vertical dotted lines mark 1, 3, 5, 7 9, and 11 times $R_h$. The five stars observed with high S/N in the present study are marked with orange stars, and the two stars observed with low S/N in the present study are marked with green circles. Previous samples from APOGEE (Abdurro'uf & Aerts 2022) and our own medium-resolution work (Pace et al. 2023, in preparation) are marked with open blue squares and small gray dots, respectively.

Figure 3 illustrates several regions of the spectra around lines of interest. A few key features are immediately discernible. First, the differences in line strengths are mainly due to differences in abundance because these stars have similar stellar parameters (Section 3.1). Second, lines of Ti and Fe exhibit only minimal differences, indicating that these stars have similar metallicities to within a factor of a few (Section 3.1). Third, one star, J1008+0001, has much stronger CH, CN, [O I], Na I, Mg I, Si I, and K I lines, while its Ba II and Eu II lines are much weaker than those in other stars (Section 4.5). Finally, J1018-0155 (along with J1010-0220 and J1018-0209; not shown) exhibits moderately strong Eu II lines, suggesting that these three stars are enhanced in *r*-process elements (Section 4.4).

We measure $v_{los}$ by cross correlating the echelle order containing the Mg I *b* triplet against a metal-poor template spectrum obtained with MIKE, using the IRAF "fxcor" task. We calculate the heliocentric velocity corrections using the IRAF "rvcorrect" task. Roederer et al. (2014a) estimated uncertainties of ≈0.7 km s$^{-1}$ for $v_{los}$ values measured by this method. Repeat observations of J1010-0220 and J1018-0209 yield consistent $v_{los}$ values that support this estimate.

## 3. Analysis

We describe our derivation of stellar parameters (Table 3) and abundances (Tables 4–7) in this section. We define the abundance of element X as $\log \varepsilon(\mathrm{X}) \equiv \log_{10}(N_\mathrm{X}/N_\mathrm{H}) + 12.0$, where $N_\mathrm{X}$ represents the number density of element X. We define the abundance ratio of X and Fe relative to the solar ratio as $[\mathrm{X/Fe}] \equiv \log_{10}(N_\mathrm{X}/N_\mathrm{Fe}) - \log_{10}(N_\mathrm{X}/N_\mathrm{Fe})_\odot$. We adopt the solar abundances, listed in Table 5, from Asplund et al. (2009). By convention, abundances or ratios denoted with the ionization state (e.g., [Fe II/H]) are understood to be the total elemental abundance as derived from transitions of that particular ionization state after Saha (1921) ionization corrections have been applied.

**Table 2**
Log of MIKE Observations

| Star name | ObsDate | UT | $t_{exp}$ (hr) | $v_{los}$ (km s$^{-1}$) | S/N@3950 Å (pix$^{-1}$) | S/N@4550 Å (pix$^{-1}$) | S/N@5200 Å (pix$^{-1}$) | S/N@6700 Å (pix$^{-1}$) |
|---|---|---|---|---|---|---|---|---|
| Stars with high-S/N observations | | | | | | | | |
| J1008+0001 | 2022/03/03 | 04:42 | 5.56 | +223.6 | 13 | 30 | 26 | 61 |
| J1010-0220 | 2021/01/12 | 08:22 | 1.11 | +209.0 | 17 | 34 | 30 | 67 |
| | 2021/01/13 | 04:58 | 2.56 | +209.8 | | | | |
| J1015-0238 | 2021/01/12 | 06:18 | 2.89 | +224.5 | 15 | 31 | 28 | 64 |
| J1018-0155 | 2021/01/13 | 07:34 | 2.47 | +222.5 | 16 | 33 | 30 | 70 |
| J1018-0209 | 2021/12/05 | 07:23 | 1.61 | +224.7 | 13 | 30 | 27 | 66 |
| | 2021/12/06 | 07:24 | 1.67 | +224.8 | | | | |
| Stars with low-S/N observations | | | | | | | | |
| J1013-0211 | 2021/01/12 | 03:59 | 0.19 | +242.1 | 3 | 8 | 8 | 19 |
| J1014-0054 | 2021/01/12 | 04:27 | 0.19 | +234.1 | 3 | 8 | 7 | 18 |

### 3.1. Model Atmospheres

We derive model atmosphere parameters using a combination of quantities measured from the spectra themselves and values adopted from external catalogs. We interpolate models from the 1D ATLAS9 grid of $\alpha$-enhanced models (Castelli & Kurucz 2003) using an interpolation code provided by A. McWilliam (2009, private communication).

We rely on abundances derived from equivalent widths (EWs) of Fe I and II lines as part of this process. We measure EWs using a semiautomated routine that fits Voigt or Gaussian line profiles to continuum-normalized spectra (Roederer et al. 2014a). Each line is inspected visually. A telluric spectrum is simultaneously compared with the stellar spectrum, and we discard any lines that appear to be contaminated by telluric absorption. These Fe I and II lines are listed in Table 4. We derive Fe abundances using a recent version of the line analysis software MOOG (Sneden 1973; Sobeck et al. 2011; 2017 version), which assumes local thermodynamic equilibrium (LTE). We adopt damping constants for collisional broadening with neutral hydrogen from Barklem et al. (2000) and Barklem & Aspelund-Johansson (2005), when available, otherwise we adopt the standard Unsöld (1955) recipe. We discard strong Fe lines with $\log(EW/\lambda) > -4.5$. The weakest lines employed in our analysis have EW $\approx$7 mÅ (Table 4).

Stellar effective temperatures ($T_{eff}$) may be derived from photometric or spectroscopic methods. We derive $T_{eff}$ values using the spectroscopic excitation balance method, and we apply a separate calibration (Frebel et al. 2013) to transform this scale, which is generally considered to be too cool, to the warmer photometric one. We begin by identifying the $T_{eff}$, log of the surface gravity ($\log g$; cm s$^{-2}$ in cgs units), microturbulent velocity parameter ($v_t$), and model metallicity ([M/H]) that meet the following set of requirements. We set $T_{eff}$ by requiring no trend between the abundance derived from Fe I lines and the lower excitation potential of each transition. We set $v_t$ by requiring no trend between the abundance derived from Fe I lines and the line strength. We set $\log g$ by requiring that the mean abundances calculated from Fe I and II lines agree within their uncertainties; in practice, these two quantities are closest at the edge of the model atmosphere grid at $\log g = 0.0$. We set [M/H] by matching the Fe abundance (from Fe I lines) plus 0.25 dex as recommended by Frebel et al. Once these values converge, we calculate a corrected $T_{eff}$ by extrapolating Equation (1) of Frebel et al. The corrected $T_{eff}$ values are $\approx$250 K warmer than the purely spectroscopic ones for these stars.

We use the corrected $T_{eff}$ to calculate a new $\log g$ from fundamental relations:

$$\log g = 4 \log T_{eff} + \log(M/M_{\odot}) - 10.61 + 0.4(BC_V + m_V - 5 \log d + 5 - 3.1E(B-V) - M_{bol,\odot}). \quad (1)$$

Here, $M$ is the mass of the star, which we assume to be $0.8 \pm 0.08\,M_{\odot}$. $BC_V$ is the bolometric correction in the $V$ band (Casagrande & VandenBerg 2014). $m_V$ is the apparent $V$ magnitude. $d$ is the distance in parsecs, which is assumed to be $86.1 \pm 2.6$ kpc (Helmi et al. 2018). We rederive $v_t$ and metallicity and iterate on the stellar parameters, including $BC_V$, until the [M/H] matches [Fe II/H] and there is no trend between the abundance derived from Fe I lines and the line strength.

Equation (1) requires an estimate of the reddening along the line of sight to each star, $E(B-V)$. We estimate $E(B-V)$ by two methods. We interpolate the dust maps presented by Schlafly & Finkbeiner (2011), which provide the $E(B-V)$ values along the line of sight, and we assume that all of the interstellar reddening lies in front of Sextans. We also estimate $E(B-V)$ using the interstellar Na I $D$ absorption (Bohlin et al. 1978; Spitzer 1978; Ferlet et al. 1985), as described in Roederer et al. (2018b). We measure the EWs by direct integration using the IRAF "splot" task. For stars J1015-0238 and J1008+0001, the ratio of the EWs of the two components of the doublet is $\approx$2:1 (120:65 and 70:35 mÅ, respectively), the same as the ratio of the $f$-values of these transitions. These lines are on the linear part of the curve of growth and thus sensitive to the reddening. For the other three stars, multiple components are present, the EWs are larger, and they are not in 2:1 ratios (J1010-0220, 220:160 mÅ; J1018-0155, 345:235 mÅ; J1018-0209, 175:100 mÅ). They are saturated and so only yield limits on the amount of interstellar absorption. The empirical relations between Na I absorption, $N(H\,I + H_2)$, and $E(B-V)$ have intrinsic scatter that corresponds to a few hundredths of a mag in $E(B-V)$. The two methods yield reasonably similar $E(B-V)$ values, which we list along with our adopted averages in Table 1. Our adopted set of stellar parameters is listed in Table 3.

We estimate the mean and uncertainty in each stellar parameter as follows. Frebel et al. (2013) estimate uncertainties

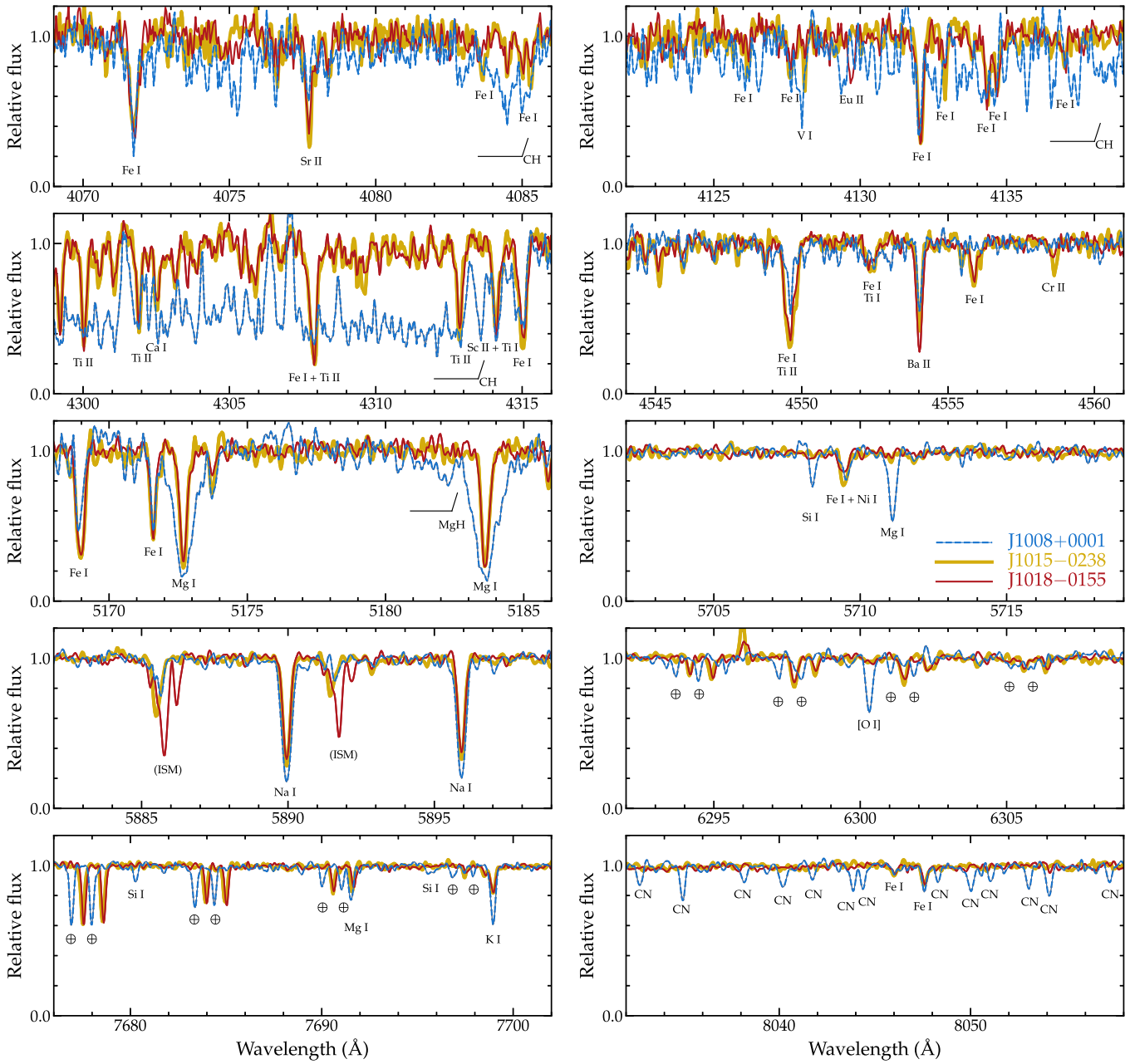


**Figure 3.** Selected regions of the MIKE spectra of three stars. Several absorption lines are identified. These three stars have similar $T_{\rm eff}$ and log $g$, so the differences in the line strengths mainly reflect abundance differences. Several interstellar medium (ISM) and $O_2$ telluric lines (⊕) are detected and marked. The telluric lines shift in velocity relative to the stellar lines, and they are marked at their approximate wavelengths in J1008+0001.

**Table 3**
Model Atmosphere Parameters

| Star Name | $T_{\rm eff}$ (K) | log $g$ | $v_{\rm t}$ (km s$^{-1}$) | [M/H][a] | [Fe I/H][b] |
|---|---|---|---|---|---|
| J1008+0001 | 4405 | 1.07 | 2.25 | −3.43 | −2.97 |
| J1010-0220 | 4405 | 0.79 | 2.15 | −3.03 | −3.34 |
| J1015-0238 | 4441 | 0.79 | 2.35 | −2.73 | −2.64 |
| J1018-0155 | 4423 | 0.72 | 2.45 | −2.89 | −2.81 |
| J1018-0209 | 4396 | 0.67 | 2.45 | −2.86 | −2.75 |

**Notes.**
[a] [M/H] ≡ [Fe II/H].
[b] Includes NLTE correction.

in $T_{\rm eff}$ of ≈150 K using their method. For log $g$, we draw $10^4$ samples from each input parameter in the log $g$ calculation, assuming Gaussian uncertainties. The statistical uncertainty associated with this method is ≈0.09 dex. The systematic uncertainty is certainly larger, ∼0.25 dex or so (Jofré et al. 2019). For a given $T_{\rm eff}$ and log $g$, the uncertainty in $v_{\rm t}$ is ≈0.2 km s$^{-1}$ and the uncertainty in [M/H] is ≈0.2 dex.

The LTE [Fe/H] ratios derived from Fe I and Fe II lines are not forced into agreement using this method. Non-LTE (NLTE) overionization of neutral Fe causes the Fe abundance from Fe I lines to be underestimated (Thévenin & Idiart 1999). NLTE corrections for Fe II lines are generally negligible. NLTE corrections are available for ≈25 of the Fe I lines for which we have measured EWs. We evaluate these corrections by

**Table 4**
Line Atomic Data and Derived Abundances

| Species | $\lambda$ | E.P. | log($gf$) | log($gf$) unc. | log($gf$) references | J1008+0001 | | | | J1010-0220 | | | |
|---|---|---|---|---|---|---|---|---|---|---|---|---|---|
| | | | | | | EW | U.L. flag | log $\epsilon$ (LTE) | NLTE corr. | EW | U.L. flag | log $\epsilon$ (LTE) | NLTE corr. |
| | Å | (eV) | | | | (mÅ) | | | | (mÅ) | | | |
| Li I | 6707.80 | 0.00 | 0.17 | 0.01 | 1 | ⋯ | < | 0.10 | +0.15 | ⋯ | < | 0.40 | +0.15 |
| O I | 6300.30 | 0.00 | −9.82 | 0.03 | 2 | ⋯ | ⋯ | 8.07 | ⋯ | ⋯ | < | 6.70 | ⋯ |
| O I | 6363.78 | 0.02 | −10.26 | 0.03 | 2 | ⋯ | ⋯ | 8.08 | ⋯ | ⋯ | ⋯ | ⋯ | ⋯ |
| Na I | 5682.63 | 2.10 | −0.71 | 0.01 | 2 | 52.2 | ⋯ | 4.96 | −0.13 | ⋯ | ⋯ | ⋯ | ⋯ |
| Na I | 5688.19 | 2.10 | −0.41 | 0.01 | 2 | 69.9 | ⋯ | 4.91 | −0.16 | ⋯ | ⋯ | ⋯ | ⋯ |

**Note.** The complete version of Table 4 is available in machine-readable form in the online edition of the journal. A small section is shown here to illustrate its form and content.

**References.** 1: Smith et al. (1998) using HFS from Kurucz (2011); 2: Kramida et al. (2021); 3: Pehlivan Rhodin et al. (2017); 4: Kramida et al. (2021), using HFS from VALD3 (Piskunov et al.é (1995), Pakhomov et al. (2019); 5: Den Hartog et al. (2023); 6: Den Hartog et al. (2021); 7: Lawler & Dakin (1989), using HFS from Kurucz (2011); 8: Lawler et al. (2013); 9: Pickering et al. (2001), using corrections given in Pickering et al. (2002); 10: Wood et al. (2013); 11: Lawler et al. (2014), including HFS; 12: Wood et al. (2014a), including HFS; 13: Sobeck et al. (2007); 14: Lawler et al. (2017); 15: Den Hartog et al. (2011), including HFS; 16: O'Brian et al. (1991); 17: Den Hartog et al. (2014); 18: Ruffoni et al. (2014); 19: Belmonte et al. (2017); 20: Blackwell et al. (1982); 21: Melendez & Barbuy (2009); 22: Den Hartog et al. (2019); 23: Lawler et al. (2015), including HFS; 24: Wood et al. (2014b); 25: Roederer & Lawler (2012); 26: Biémont et al. (2011); 27: Ljung et al. (2006); 28: Kramida et al. (2021), using HFS/IS from McWilliam (1998) or other sources when available; 29: Lawler et al. (2001a), using HFS from Ivans et al. (2006) when available; 30: Lawler et al. (2009); 31: Li et al. (2007), using HFS from Sneden et al. (2009); 32: Den Hartog et al. (2003); 33: Lawler et al. (2006), using HFS/IS from Roederer et al. (2008); 34: Lawler et al. (2001b), using HFS/IS from Ivans et al. (2006); 35: Wickliffe et al. (2000); 36: Biemont et al. (2000), using HFS/IS from Roederer et al. (2012).

(This table is available in its entirety in machine-readable form.)

interpolating the precomputed grids presented in the INSPECT database (Bergemann et al. 2012; Lind et al. 2012). The NLTE corrections range from +0.10 to +0.14 for these five stars. [Fe II/Fe I] ionization equilibrium is achieved within 1.8$\sigma$ after including these NLTE corrections. We adopt the NLTE-corrected Fe abundance from Fe I lines when constructing abundance ratios of various elements relative to Fe (i.e., [X/Fe]).

### 3.2. Abundance Derivations

We use the MOOG "abfind" driver to derive abundances from EWs of Mg I, Ca I, Ti I and II, Cr I and II, Fe I and II, Ni I, and some Zn I lines. Lines of these species are unblended, are comprised of a single or dominant isotope or do not exhibit any significant line broadening by isotope shifts (IS), and do not exhibit any significant line broadening by hyperfine structure (HFS). All other abundances are derived by matching synthetic spectra generated using the MOOG "synth" driver to the observed spectrum. We produce line lists for these synthetic spectra using the LINEMAKE code (Placco et al. 2021b). We assume $^{12}C/^{13}C = 4$, all N is $^{14}N$, and $r$-process isotopic ratios (Sneden et al. 2008) in our syntheses. Upper limits (U.L.) are reported for a few key species based on the non-detection of one or more lines in our spectra. Table 4 reports the wavelengths ($\lambda$), excitation potentials (E.P.), log($gf$) values and their references, along with the EWs and LTE abundances for each line in each star.

We apply NLTE corrections, when available and potentially non-negligible, to the LTE abundances of each line of Li I (Lind et al. 2009), Na I (Lind et al. 2011), Mg I (Osorio et al. 2015; Osorio & Barklem 2016), Al I (Nordlander & Lind 2017), Si I (Shi et al. 2009), K I (Takeda et al. 2002), and Pb I (Mashonkina et al. 2012). The Li I, Na I, and Mg I NLTE corrections are accessed through the INSPECT database. The stellar parameters occasionally lie beyond the edge of precomputed grids (usually in $T_{\rm eff}$ or log $g$, with edges at 4500 K or 1.0 dex, respectively), and in these cases, we adopt the correction at the nearest point on the grid. Table 4 lists the line-by-line NLTE corrections, and Tables 5–7 list the NLTE-corrected mean abundances.

We compute abundance uncertainties by drawing $10^3$ resamples of the model atmosphere parameters, log($gf$) values, and EWs (or approximations to the EWs for lines whose abundance was derived using spectrum synthesis), assuming Gaussian uncertainties. The uncertainties on the model atmosphere parameters are discussed in Section 3.1. The uncertainties in the log($gf$) values are taken from the grades assigned by the National Institutes of Standards and Technology (NIST) Atomic Spectra Database (ASD, version 5.9; Kramida et al. 2021) or the original source references listed in Table 4. We assume a 5% uncertainty in the EWs, or a 5 mÅ minimum uncertainty in the case of weak lines, which accounts for continuum placement and unidentified weak blends. We also include a wavelength-dependent component of EW uncertainty that reflects the low S/N at blue wavelengths, which we empirically determine to be $\sigma_{\rm EW} = 10^{24}\lambda^{-6.4}$, where the wavelength, $\lambda$, is measured in angstroms and $\sigma_{\rm EW}$ is measured in milliangstroms. This component of the uncertainty is ≈9 mÅ at 4000 Å, ≈4 mÅ at 4500 Å, ≈2 mÅ at 5000 Å, and <1 mÅ at 6000 Å. The mean abundance of each element is recomputed for each resample, and the final abundance uncertainties reported in Tables 5–7 represent the 16th and 84th percentiles (i.e., 1$\sigma$ range) of the distributions, which are roughly symmetric in most cases.

The uncertainties are generally smallest when the abundance is derived from several lines with $\lambda \gtrsim 4500$ Å, where the S/N is highest. There are several heavy elements, including Ce, Pr, Sm, and Dy, whose abundances are derived from a small number (1 or 2) of very weak (EW < 10 mÅ or so) lines in the blue part of the spectrum ($\lambda < 4500$ Å). The abundances are in agreement when multiple lines of one of these elements are detected in a star, which boosts our confidence in the

**Table 5**
Derived Abundances (Part 1 of 3)

| | | | J1008+0001 | | | | | J1010-0220 | | | | |
|---|---|---|---|---|---|---|---|---|---|---|---|---|
| Species | $Z$ | $\log \varepsilon_\odot$ | $\log \varepsilon$(X) | [X/Fe] | $\sigma(\log \varepsilon$(X)) | $\sigma$([X/Fe]) | $N$ | $\log \varepsilon$(X) | [X/Fe] | $\sigma(\log \varepsilon$(X)) | $\sigma$([X/Fe]) | $N$ |
| Li I | 3 | ⋯ | <0.25 | ⋯ | ⋯ | ⋯ | 1 | <0.55 | ⋯ | ⋯ | ⋯ | 1 |
| C (CH) | 6 | 8.43 | 7.41 | +1.95 | 0.20 | 0.20 | 1 | 5.45 | +0.36 | 0.20 | 0.20 | 1 |
| N (CN) | 7 | 7.83 | 6.70 | +1.84 | 0.30 | 0.30 | 1 | ⋯ | ⋯ | ⋯ | ⋯ | 0 |
| O I | 8 | 8.69 | 8.08 | +2.36 | 0.15 | 0.18 | 2 | <6.70 | < +1.35 | ⋯ | ⋯ | 1 |
| Na I | 11 | 6.24 | 4.86 | +1.59 | 0.13 | 0.14 | 4 | 2.61 | −0.29 | 0.29 | 0.11 | 2 |
| Mg I | 12 | 7.60 | 6.47 | +1.84 | 0.21 | 0.13 | 3 | 4.47 | +0.21 | 0.14 | 0.17 | 2 |
| Al I | 13 | 6.45 | <5.20 | < +1.72 | ⋯ | ⋯ | 2 | 3.07 | −0.04 | 0.39 | 0.28 | 1 |
| Si I | 14 | 7.51 | 6.28 | +1.74 | 0.10 | 0.18 | 13 | 4.27 | +0.10 | 0.38 | 0.36 | 1 |
| K I | 19 | 5.03 | 3.34 | +1.28 | 0.26 | 0.13 | 1 | 2.13 | +0.44 | 0.22 | 0.13 | 2 |
| Ca I | 20 | 6.34 | 3.87 | +0.50 | 0.16 | 0.09 | 14 | 3.15 | +0.15 | 0.18 | 0.12 | 6 |
| Sc II | 21 | 3.15 | −0.23 | −0.41 | 0.13 | 0.16 | 4 | −0.30 | −0.11 | 0.14 | 0.14 | 5 |
| Ti I | 22 | 4.95 | 2.40 | +0.42 | 0.27 | 0.07 | 11 | 1.58 | −0.03 | 0.31 | 0.13 | 5 |
| Ti II | 22 | 4.95 | 1.81 | −0.17 | 0.11 | 0.14 | 9 | 1.80 | +0.19 | 0.11 | 0.10 | 16 |
| V I | 23 | 3.93 | ⋯ | ⋯ | ⋯ | ⋯ | 0 | ⋯ | ⋯ | ⋯ | ⋯ | 0 |
| V II | 23 | 3.93 | ⋯ | ⋯ | ⋯ | ⋯ | 0 | ⋯ | ⋯ | ⋯ | ⋯ | 0 |
| Cr I | 24 | 5.64 | 2.64 | −0.04 | 0.25 | 0.06 | 9 | 2.01 | −0.29 | 0.27 | 0.12 | 4 |
| Cr II | 24 | 5.64 | ⋯ | ⋯ | ⋯ | ⋯ | 0 | 2.40 | +0.10 | 0.33 | 0.33 | 1 |
| Mn I | 25 | 5.43 | 2.46 | +0.00 | 0.22 | 0.09 | 3 | 1.77 | −0.32 | 0.28 | 0.20 | 1 |
| Fe I | 26 | 7.50 | 4.53 | −2.97 | 0.22 | 0.22 | 70 | 4.16 | −3.34 | 0.26 | 0.26 | 78 |
| Fe II | 26 | 7.50 | 4.07 | −3.43 | 0.14 | 0.14 | 2 | 4.47 | −3.03 | 0.11 | 0.11 | 7 |
| Co I | 27 | 4.99 | ⋯ | ⋯ | ⋯ | ⋯ | 0 | ⋯ | ⋯ | ⋯ | ⋯ | 0 |
| Ni I | 28 | 6.22 | 3.40 | +0.15 | 0.21 | 0.09 | 6 | 2.50 | −0.38 | 0.25 | 0.10 | 1 |
| Zn I | 30 | 4.56 | 2.26 | +0.67 | 0.10 | 0.23 | 2 | 1.67 | +0.45 | 0.24 | 0.34 | 2 |
| Sr II | 38 | 2.87 | −2.47 | −2.37 | 0.21 | 0.25 | 1 | −0.97 | −0.49 | 0.25 | 0.25 | 2 |
| Y II | 39 | 2.21 | ⋯ | ⋯ | ⋯ | ⋯ | 0 | −1.34 | −0.21 | 0.19 | 0.19 | 3 |
| Zr II | 40 | 2.58 | ⋯ | ⋯ | ⋯ | ⋯ | 0 | −0.62 | +0.15 | 0.26 | 0.28 | 2 |
| Ba II | 56 | 2.18 | −2.24 | −1.45 | 0.17 | 0.20 | 3 | −1.27 | −0.10 | 0.16 | 0.16 | 4 |
| La II | 57 | 1.10 | ⋯ | ⋯ | ⋯ | ⋯ | 0 | −1.76 | +0.49 | 0.22 | 0.22 | 2 |
| Ce II | 58 | 1.58 | ⋯ | ⋯ | ⋯ | ⋯ | 0 | −1.35 | +0.42 | 0.50 | 0.50 | 2 |
| Pr II | 59 | 0.72 | ⋯ | ⋯ | ⋯ | ⋯ | 0 | ⋯ | ⋯ | ⋯ | ⋯ | 0 |
| Nd II | 60 | 1.42 | ⋯ | ⋯ | ⋯ | ⋯ | 0 | −1.41 | +0.51 | 0.25 | 0.26 | 2 |
| Sm II | 62 | 0.96 | ⋯ | ⋯ | ⋯ | ⋯ | 0 | −1.53 | +0.86 | 0.50 | 0.50 | 2 |
| Eu II | 63 | 0.52 | < −2.40 | < +0.05 | ⋯ | ⋯ | 2 | −2.12 | +0.70 | 0.20 | 0.21 | 3 |
| Dy II | 66 | 1.10 | ⋯ | ⋯ | ⋯ | ⋯ | 0 | ⋯ | ⋯ | ⋯ | ⋯ | 0 |
| Pb I | 82 | 2.04 | <0.60 | < +1.53 | ⋯ | ⋯ | 1 | <0.29 | < +1.59 | ⋯ | ⋯ | 1 |

**Notes.** [Fe/H] is given instead of [X/Fe] for Fe. The C abundances have been corrected (by +0.41 and +0.75 dex) to the natal abundances according to the stellar evolution corrections presented by Placco et al. (2014). A single C abundance is derived by spectrum synthesis of the region from 4290–4330 Å. NLTE corrections have been applied to the Li, Na, Mg, Al, Si, K, Fe I, and Pb abundances; see Table 4 for corrections and the text for references.

legitimacy of their detection despite the relatively large uncertainties.

## 4. Results

In this section, we present our abundance results and compare them with previous work. Our sample contains no stars in common with previous high-resolution abundance studies. Figure 4 shows the abundance ratios for the stars in our sample, previous results for Sextans stars, and metal-poor field stars in the solar neighborhood. Several studies have reobserved or reanalyzed spectra of Sextans stars. We display these results in Figure 4 with lines connecting the different results for individual stars.

### 4.1. $\alpha$ Elements: O, Mg, Si, Ca, and Ti

We detect five $\alpha$ elements in our sample: O ($Z = 8$), Mg ($Z = 12$), Si ($Z = 14$), Ca ($Z = 20$), and Ti ($Z = 22$). We detect O only in J1008+0001, which we discuss separately in Section 4.5. The mean [Mg/Fe], [Si/Fe], [Ca/Fe], and [Ti/Fe] ratios found in the other four stars in our sample, weighted by their inverse-squared uncertainties, are $+0.27 \pm 0.08$, $+0.15 \pm 0.16$, $+0.10 \pm 0.05$, and $+0.14 \pm 0.05$, respectively. The weighted mean [$\alpha$/Fe] ratio in these four stars is $+0.12 \pm 0.03$. As shown in Figure 4, these ratios are enhanced relative to the solar ratios, but they are a few tenths of a dex low relative to the mean ratios in field red giants with similar low metallicities. These [$\alpha$/Fe] ratios could indicate a deficiency of metals produced by the highest-mass stars (e.g., McWilliam et al. 2013).

Our result is broadly consistent with abundances derived previously from high-resolution spectra of the most metal-poor Sextans stars known (Shetrone et al. 2001; Aoki et al. 2009; Tafelmeyer et al. 2010; Aoki et al. 2020; Mashonkina et al. 2022). Our mean [Mg/Fe] abundance is in agreement with that derived by Mashonkina et al. from their homogeneous NLTE reanalysis of 10 Sextans stars with $-3.2 \leqslant$ [Fe/H] $\leqslant -2.6$, [Mg/Fe] $= +0.27 \pm 0.08$; our value is also in agreement with their LTE value, [Mg/Fe] $= +0.24 \pm 0.08$. Our mean [Ca/Fe] abundance is lower than the NLTE derived by Mashonkina et al. [Ca/Fe] $= +0.31 \pm 0.06$, but it is in agreement with their LTE value, [Ca/Fe] $= +0.16 \pm 0.06$.

**Table 6**
Derived Abundances (Part 2 of 3)

| | | | J1015-0238 | | | | | J1018-0155 | | | | |
|---|---|---|---|---|---|---|---|---|---|---|---|---|
| Species | $Z$ | $\log\varepsilon_\odot$ | $\log\varepsilon$(X) | [X/Fe] | $\sigma(\log\varepsilon(X))$ | $\sigma$([X/Fe]) | $N$ | $\log\varepsilon$(X) | [X/Fe] | $\sigma(\log\varepsilon(X))$ | $\sigma$([X/Fe]) | $N$ |
| Li I | 3 | ... | <0.21 | ... | ... | ... | 1 | <0.51 | ... | ... | ... | 1 |
| C (CH) | 6 | 8.43 | 5.77 | −0.22 | 0.20 | 0.20 | 1 | 5.37 | −0.25 | 0.20 | 0.20 | 1 |
| N (CN) | 7 | 7.83 | ... | ... | ... | ... | 0 | ... | ... | ... | ... | 0 |
| O I | 8 | 8.69 | <6.70 | < +0.65 | ... | ... | 1 | <6.80 | < +0.92 | ... | ... | 1 |
| Na I | 11 | 6.24 | 3.62 | +0.02 | 0.38 | 0.16 | 2 | 3.50 | +0.07 | 0.35 | 0.15 | 2 |
| Mg I | 12 | 7.60 | 5.19 | +0.23 | 0.18 | 0.17 | 3 | 5.11 | +0.32 | 0.14 | 0.14 | 2 |
| Al I | 13 | 6.45 | 3.92 | +0.11 | 0.39 | 0.25 | 1 | 4.38 | +0.74 | 0.38 | 0.24 | 1 |
| Si I | 14 | 7.51 | 5.07 | +0.20 | 0.43 | 0.37 | 1 | 4.71 | +0.01 | 0.40 | 0.36 | 1 |
| K I | 19 | 5.03 | 2.42 | +0.03 | 0.21 | 0.07 | 2 | 2.40 | +0.18 | 0.20 | 0.07 | 2 |
| Ca I | 20 | 6.34 | 3.82 | +0.12 | 0.17 | 0.09 | 15 | 3.65 | +0.12 | 0.16 | 0.10 | 12 |
| Sc II | 21 | 3.15 | 0.31 | −0.20 | 0.11 | 0.11 | 9 | 0.17 | −0.17 | 0.11 | 0.10 | 9 |
| Ti I | 22 | 4.95 | 2.35 | +0.04 | 0.29 | 0.07 | 16 | 2.08 | −0.06 | 0.29 | 0.09 | 10 |
| Ti II | 22 | 4.95 | 2.58 | +0.27 | 0.11 | 0.09 | 25 | 2.27 | +0.13 | 0.09 | 0.09 | 20 |
| V I | 23 | 3.93 | 0.94 | −0.35 | 0.31 | 0.11 | 3 | 0.87 | −0.25 | 0.32 | 0.16 | 3 |
| V II | 23 | 3.93 | 1.22 | −0.07 | 0.17 | 0.17 | 2 | 1.05 | −0.07 | 0.30 | 0.29 | 1 |
| Cr I | 24 | 5.64 | 2.77 | −0.23 | 0.27 | 0.07 | 7 | 2.45 | −0.38 | 0.25 | 0.06 | 8 |
| Cr II | 24 | 5.64 | 3.07 | +0.07 | 0.15 | 0.12 | 2 | 2.67 | −0.16 | 0.28 | 0.27 | 1 |
| Mn I | 25 | 5.43 | 2.38 | −0.41 | 0.23 | 0.09 | 3 | 2.08 | −0.54 | 0.22 | 0.10 | 3 |
| Fe I | 26 | 7.50 | 4.86 | −2.64 | 0.24 | 0.24 | 115 | 4.69 | −2.81 | 0.24 | 0.24 | 107 |
| Fe II | 26 | 7.50 | 4.77 | −2.73 | 0.11 | 0.11 | 10 | 4.61 | −2.89 | 0.11 | 0.11 | 11 |
| Co I | 27 | 4.99 | 2.06 | −0.29 | 0.34 | 0.16 | 1 | 1.84 | −0.34 | 0.31 | 0.14 | 1 |
| Ni I | 28 | 6.22 | 3.56 | −0.02 | 0.21 | 0.08 | 6 | 3.30 | −0.11 | 0.23 | 0.13 | 5 |
| Zn I | 30 | 4.56 | 2.24 | +0.32 | 0.11 | 0.24 | 2 | 1.83 | +0.08 | 0.17 | 0.27 | 2 |
| Sr II | 38 | 2.87 | 0.31 | +0.08 | 0.18 | 0.19 | 2 | −0.72 | −0.78 | 0.25 | 0.25 | 2 |
| Y II | 39 | 2.21 | −0.80 | −0.37 | 0.12 | 0.13 | 3 | −1.39 | −0.79 | 0.16 | 0.17 | 2 |
| Zr II | 40 | 2.58 | 0.01 | +0.07 | 0.15 | 0.15 | 3 | −0.52 | −0.29 | 0.21 | 0.21 | 3 |
| Ba II | 56 | 2.18 | −1.59 | −1.13 | 0.15 | 0.16 | 4 | −0.94 | −0.31 | 0.15 | 0.15 | 4 |
| La II | 57 | 1.10 | ... | ... | ... | ... | 0 | −1.71 | +0.00 | 0.23 | 0.24 | 5 |
| Ce II | 58 | 1.58 | ... | ... | ... | ... | 0 | −1.20 | +0.03 | 0.26 | 0.27 | 2 |
| Pr II | 59 | 0.72 | ... | ... | ... | ... | 0 | −1.62 | +0.47 | 0.27 | 0.28 | 1 |
| Nd II | 60 | 1.42 | ... | ... | ... | ... | 0 | −1.15 | +0.24 | 0.20 | 0.20 | 3 |
| Sm II | 62 | 0.96 | ... | ... | ... | ... | 0 | −1.73 | +0.12 | 0.45 | 0.45 | 1 |
| Eu II | 63 | 0.52 | < −2.70 | < −0.58 | ... | ... | 2 | −1.96 | +0.33 | 0.15 | 0.15 | 3 |
| Dy II | 66 | 1.10 | ... | ... | ... | ... | 0 | −1.06 | +0.65 | 0.43 | 0.44 | 1 |
| Pb I | 82 | 2.04 | <0.10 | < +0.70 | ... | ... | 1 | <0.05 | < +0.82 | ... | ... | 1 |

**Notes.** [Fe/H] is given instead of [X/Fe] for Fe. The C abundances have been corrected (by +0.77 and +0.76 dex) to the natal abundances according to the stellar evolution corrections presented by Placco et al. (2014). A single C abundance is derived by spectrum synthesis of the region from 4290–4330 Å. NLTE corrections have been applied to the Li, Na, Mg, Al, Si, K, Fe I, and Pb abundances; see Table 4 for corrections and the text for references.

Previous studies generally agree that there is a decline in the [$\alpha$/Fe] ratios at higher metallicities. There is mild disagreement about the placement of the knee in the [$\alpha$/Fe] versus [Fe/H] relation. Reichert et al. (2020) found a hint that there may be two knees in the [Mg/Fe] versus [Fe/H] relation, at [Fe/H] $= -2.5$ and $-2.0$, which could be a consequence of the accretion history of Sextans. Mashonkina et al. (2022) discuss this issue in more detail. Our sample only includes stars with [Fe/H] $< -2.6$, so we are unable to contribute to this particular debate.

### 4.2. Other Light Elements: Li, C, N, Na, Al, and K

Li ($Z = 3$) is not detected in any star in our sample. The upper limits on the Li abundances, $\log\varepsilon$(Li) <0.6, are lower than the traditional Spite & Spite (1982) plateau value, $\log\varepsilon$(Li) ≈2.2, and the slight downturn in Li abundances found in unevolved stars with [Fe/H] $< -2.8$ (Sbordone et al. 2010). The low Li abundances in our stars are consistent with the well-established phenomenon wherein Li in the atmosphere is diluted as the base of the convective zone deepens to hotter layers during normal stellar evolution up the red giant branch.

C ($Z = 6$) is detected in all five stars in our sample via the CH A-X ($G$) band. We derive the C abundance in each star by synthesizing the CH features in the 4290–4330 Å wavelength region, using lines from Masseron et al. (2014). The C abundances have been corrected to account for CN processing during normal stellar evolution (Placco et al. 2014), so the values presented in Tables 5–7 reflect the natal C abundances. The corrections for four of the stars are ≈ +0.75 dex, and their corrected [C/Fe] ratios are solar to within a factor of ≈2. Only one of the five stars, J1008+0001, is C enhanced. Its evolutionary correction is +0.41 dex, yielding a natal [C/Fe] $= +1.95 \pm 0.20$. We discuss this carbon-enhanced metal-poor (CEMP) star in Section 4.5.

N ($Z = 7$) is detected only in the CEMP star in our sample via the CN A-X (red system) bands. We derive the N abundance from the CN features in the 8000–8100 Å wavelength region, using lines from Sneden et al. (2014). The natal N abundance in this star is difficult to infer, because a wide range of initial—lower—N abundances can yield similar surface N abundances as

**Table 7**
Derived Abundances (Part 3 of 3)

| | | | J1018-0209 | | | | |
|---|---|---|---|---|---|---|---|
| Species | $Z$ | $\log \varepsilon_{\odot}$ | $\log \varepsilon$(X) | [X/Fe] | $\sigma(\log \varepsilon(X))$ | $\sigma$([X/Fe]) | $N$ |
| Li I | 3 | ⋯ | <0.25 | ⋯ | ⋯ | ⋯ | 1 |
| C (CH) | 6 | 8.43 | 5.34 | −0.34 | 0.20 | 0.20 | 1 |
| N (CN) | 7 | 7.83 | ⋯ | ⋯ | ⋯ | ⋯ | 0 |
| O I | 8 | 8.69 | <6.90 | < +0.96 | ⋯ | ⋯ | 1 |
| Na I | 11 | 6.24 | 3.25 | −0.24 | 0.24 | 0.08 | 3 |
| Mg I | 12 | 7.60 | 5.15 | +0.30 | 0.15 | 0.13 | 5 |
| Al I | 13 | 6.45 | 3.30 | −0.40 | 0.40 | 0.28 | 1 |
| Si I | 14 | 7.51 | 4.98 | +0.22 | 0.26 | 0.26 | 2 |
| K I | 19 | 5.03 | 2.36 | +0.08 | 0.21 | 0.09 | 1 |
| Ca I | 20 | 6.34 | 3.63 | +0.04 | 0.16 | 0.10 | 13 |
| Sc II | 21 | 3.15 | 0.08 | −0.32 | 0.11 | 0.11 | 8 |
| Ti I | 22 | 4.95 | 2.05 | −0.15 | 0.30 | 0.07 | 11 |
| Ti II | 22 | 4.95 | 2.19 | −0.01 | 0.10 | 0.09 | 20 |
| V I | 23 | 3.93 | 0.60 | −0.58 | 0.34 | 0.19 | 1 |
| V II | 23 | 3.93 | 1.18 | +0.00 | 0.23 | 0.23 | 2 |
| Cr I | 24 | 5.64 | 2.53 | −0.36 | 0.27 | 0.06 | 5 |
| Cr II | 24 | 5.64 | ⋯ | ⋯ | ⋯ | ⋯ | 0 |
| Mn I | 25 | 5.43 | 2.07 | −0.61 | 0.22 | 0.09 | 3 |
| Fe I | 26 | 7.50 | 4.75 | −2.75 | 0.25 | 0.25 | 113 |
| Fe II | 26 | 7.50 | 4.64 | −2.86 | 0.10 | 0.10 | 13 |
| Co I | 27 | 4.99 | ⋯ | ⋯ | ⋯ | ⋯ | 0 |
| Ni I | 28 | 6.22 | 3.32 | −0.15 | 0.23 | 0.07 | 4 |
| Zn I | 30 | 4.56 | 2.00 | +0.19 | 0.12 | 0.26 | 2 |
| Sr II | 38 | 2.87 | −0.73 | −0.85 | 0.25 | 0.23 | 2 |
| Y II | 39 | 2.21 | −1.21 | −0.67 | 0.14 | 0.15 | 3 |
| Zr II | 40 | 2.58 | −0.58 | −0.41 | 0.23 | 0.24 | 1 |
| Ba II | 56 | 2.18 | −0.87 | −0.30 | 0.18 | 0.17 | 5 |
| La II | 57 | 1.10 | −1.77 | −0.12 | 0.19 | 0.20 | 2 |
| Ce II | 58 | 1.58 | −1.37 | −0.20 | 0.50 | 0.50 | 2 |
| Pr II | 59 | 0.72 | ⋯ | ⋯ | ⋯ | ⋯ | 0 |
| Nd II | 60 | 1.42 | ⋯ | ⋯ | ⋯ | ⋯ | 0 |
| Sm II | 62 | 0.96 | −1.64 | +0.15 | 0.50 | 0.50 | 2 |
| Eu II | 63 | 0.52 | −2.06 | +0.17 | 0.20 | 0.21 | 3 |
| Dy II | 66 | 1.10 | ⋯ | ⋯ | ⋯ | ⋯ | 0 |
| Pb I | 82 | 2.04 | <0.00 | < +0.71 | ⋯ | ⋯ | 1 |

**Notes.** [Fe/H] is given instead of [X/Fe] for Fe. The C abundance has been corrected (by +0.77 dex) to the natal abundance according to the stellar evolution corrections presented by Placco et al. (2014). A single C abundance is derived by spectrum synthesis of the region from 4290–4330 Å. NLTE corrections have been applied to the Li, Na, Mg, Al, Si, K, Fe I, and Pb abundances; see Table 4 for corrections and the text for references.

CN-processed and N-enhanced material is dredged up during stellar evolution (Placco et al. 2014). We adopt the current surface abundance, $[\mathrm{N/Fe}] = +1.84 \pm 0.30$, as the natal abundance, but we recommend that it be interpreted with caution.

Na ($Z = 11$) is detected in all five stars in our sample. The NLTE-corrected [Na/Fe] ratios are solar to within a factor of ≈2 in four of the five stars. They fall within the range of metal-poor field stars and previously examined stars in the inner region of Sextans. The [Na/Fe] ratio is highly enhanced, $[\mathrm{Na/Fe}] = +1.59 \pm 0.14$, in the CEMP star.

Al ($Z = 13$) is detected in all five stars. We apply NLTE corrections to the LTE abundances in Tables 5–7. Figure 4, however, only shows the LTE abundances for the sake of comparing with literature data, which generally have not been corrected for NLTE. The [Al/Fe] ratios are within the range of field stars and other Sextans stars. Two of the stars in our sample exhibit solar [Al/Fe] ratios in NLTE, which is common among stars with $[\mathrm{Fe/H}] < -2$ (e.g., Andrievsky et al. 2008; Roederer & Lawler 2021). One star, J1018-0155, exhibits significantly enhanced $[\mathrm{Al/Fe}] = +0.74 \pm 0.24$ in NLTE. Another star, J1018-0209, is moderately deficient in Al, with $[\mathrm{Al/Fe}] = -0.40 \pm 0.28$. No other abundance anomalies are found among light elements in either of these two stars, and we lack a satisfactory explanation for the differences in their Al abundances. There is no reliable Al abundance indicator in our spectrum of the CEMP star. The lines of the resonance Al I doublet at 3944 and 3961 Å are detected but heavily blended with CH features. The high-excitation Al I doublet at 6696 and 6698 Å is weak and undetected in our spectrum. We derive an upper limit on the Al abundance in this star, $[\mathrm{Al/Fe}] < +1.72$, using the latter doublet.

K ($Z = 19$) is detected in all five stars. K has not been detected previously in any star in Sextans. The mean NLTE [K/Fe] ratio in the four non-CEMP stars, $+0.10 \pm 0.04$, falls within the same range as the mean [$\alpha$/Fe] ratios in these stars. These [K/Fe] ratios also overlap with those of halo stars at similar metallicities. The CEMP star exhibits highly enhanced K, $[\mathrm{K/Fe}] = +1.28 \pm 0.13$. This value is higher than that for

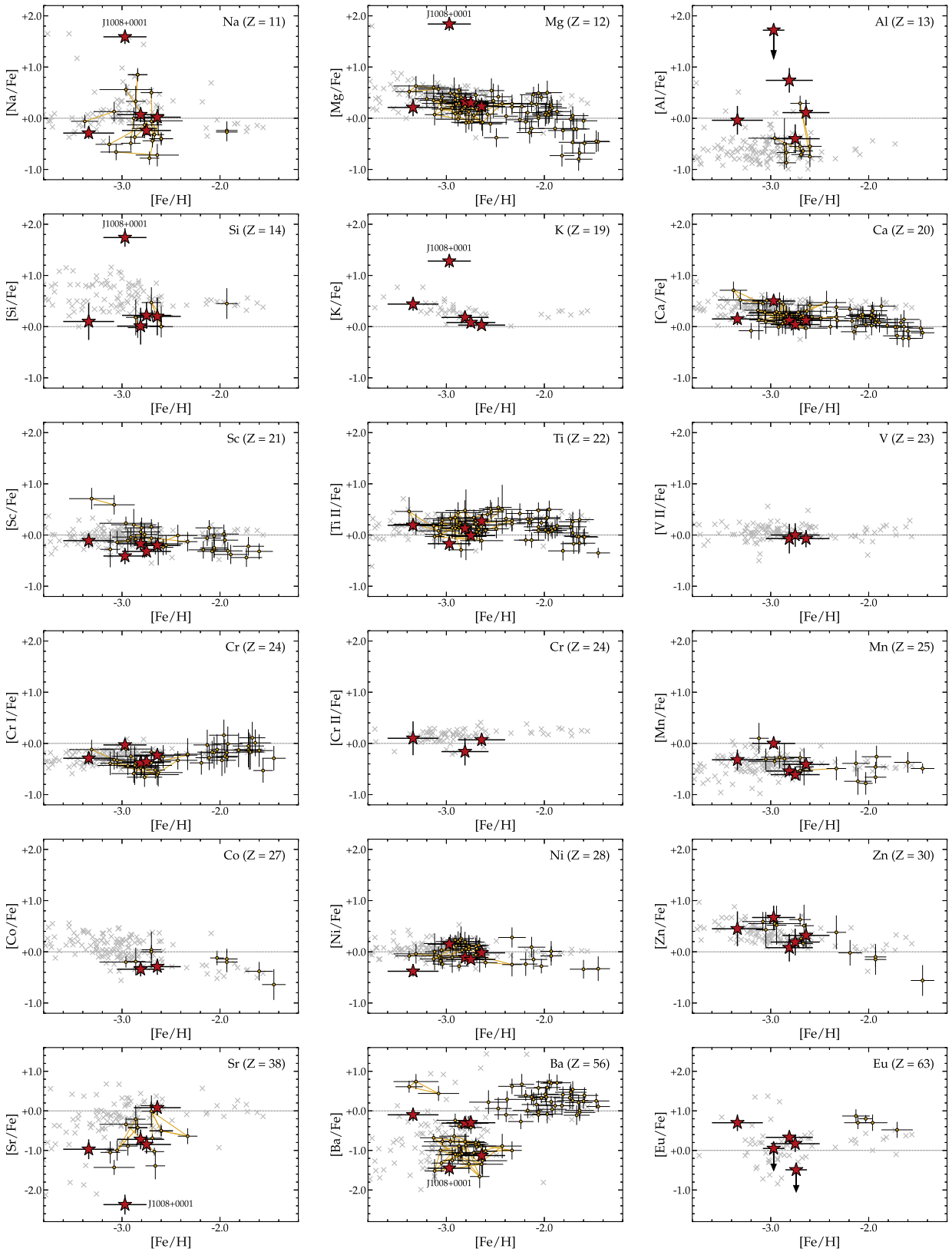


**Figure 4.** Abundance ratios for stars in our sample (large red stars) compared with previous results for Sextans stars (yellow circles) and metal-poor field stars (gray crosses). Yellow lines connect stars reobserved or reanalyzed by previous studies. The Sextans sample includes results from Shetrone et al. (2001), Aoki et al. (2009), Tafelmeyer et al. (2010), Honda et al. (2011), Mashonkina et al. (2017, 2022), Aoki et al. (2020), and Lucchesi et al. (2020). The field sample includes red giants ($T_{\rm eff} < 5400$ K) from Cayrel et al. (2004), Lai et al. (2008), Yong et al. (2013), Roederer et al. (2014a), and Ou et al. (2020). Abundances in the comparison samples have been computed in LTE, except for Na in most studies, and most abundances in the 11 stars studied by Mashonkina et al. (2017, 2022). The panels are arranged in order of increasing atomic number ($Z$).

any star listed in the JINABase abundance database (Abohalima & Frebel 2018).

### 4.3. Iron-group Elements: Sc–Zn

Several iron-group elements, including Ti ($Z = 22$), V ($Z = 23$), and Cr ($Z = 24$), are detected in multiple ionization states. The differences in the abundances derived from these different states are generally consistent from one star to another: $\approx +0.2$ dex for Ti (with the exception of J1008 +0001), $\approx +0.3$ dex for V, and $\approx +0.3$ dex for Cr. The ions yield higher abundances than the neutrals. These differences are broadly consistent with previous NLTE calculations that suggest the differences in Ti and Cr can be attributed to NLTE overionization of the minority neutral species in cool, metal-poor giants (e.g., Bergemann & Cescutti 2010; Sitnova et al. 2016). Similar NLTE calculations for V have not been made. The ions should yield more reliable abundances of these species.

The mean [X/Fe] ratios of most iron-group elements are within ≈0.2 dex of the solar ratios: [Sc/Fe] $= -0.21 \pm 0.06$, [Ti/Fe] $= +0.14 \pm 0.05$, [V/Fe] $= -0.04 \pm 0.16$, [Cr/Fe] $= -0.02 \pm 0.12$, and [Ni/Fe] $= -0.15 \pm 0.04$. The mean [Mn/Fe] and [Co/Fe] ratios are deficient relative to the solar ratios, $-0.31 \pm 0.05$ and $-0.33 \pm 0.13$, respectively. Both Mn and Co are detected only in their neutral states, which could underestimate their abundances by several tenths of a dex (e.g., Bergemann & Gehren 2008; Bergemann et al. 2010). The mean [Zn/Fe] ratio is enhanced relative to the solar ratio, $+0.30 \pm 0.13$. As shown in Figure 4, all of these ratios overlap with the range of ratios in stars in the inner region of Sextans and metal-poor field stars.

Cowan et al. (2020) and Sneden et al. (2023) have shown that the [Sc/Fe], [Ti/Fe], and [V/Fe] ratios are correlated in metal-poor field stars. The mean [Sc/Fe], [Ti/Fe], and [V/Fe] ratios in our Sextans stars are lower by ≈0.1–0.2 dex than the means in the metal-poor field star samples. These three ratios in our Sextans stars match the low end of the correlations found by Sneden et al., as shown in their Figure 7. This finding suggests that the supernovae that produced the bulk of the $\alpha$ and iron-group elements in our Sextans stars were not atypical, yet they produced slight deficiencies in most elements relative to Fe. We encourage new theoretical investigations of supernova yields to better understand this behavior.

### 4.4. Heavy Elements: Sr–Pb

We detect Sr ($Z = 38$) and Ba ($Z = 56$) in all stars in our sample, and elements heavier than Ba can be detected in three of the five stars. As shown in Figure 4, four of the five [Sr/Fe] ratios are comparable to those found in Sextans stars examined previously, $-0.85 \leqslant$ [Sr/Fe] $\leqslant +0.08$. In contrast, the [Sr/Fe] ratio in the CEMP star, $-2.37 \pm 0.25$, is ≈1 dex lower than any other star known in Sextans. The [Ba/Fe] ratios in three of the stars, $-0.31 \leqslant$ [Ba/Fe] $\leqslant -0.10$, are higher than most other Sextans stars with [Fe/H] $< -2.6$. The two other stars, including the CEMP star, exhibit [Ba/Fe] ratios nearly one dex lower.

Figure 5 illustrates the heavy-element abundance pattern in the five Sextans stars. The solar system *r*-process and *s*-process abundance patterns, normalized to the Ba abundance in each star, are shown for comparison (Prantzos et al. 2020). The *s*-process pattern is disfavored. Furthermore, enhanced Pb

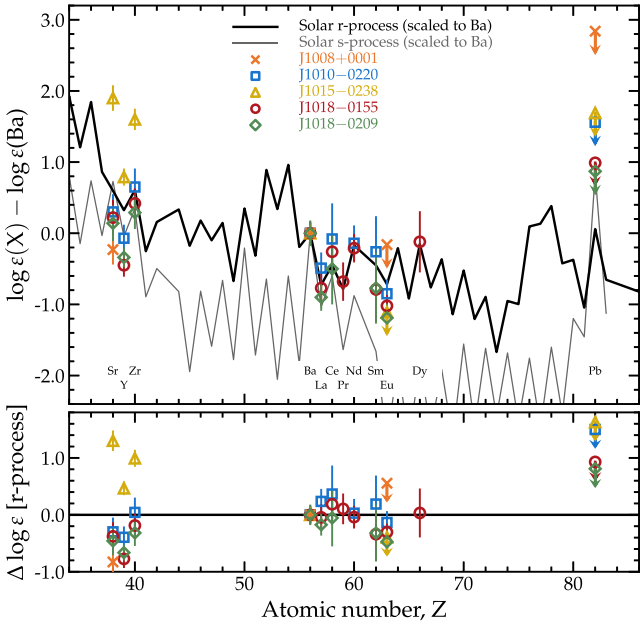


**Figure 5.** Heavy-element abundance patterns in the five Sextans stars. The top panel illustrates the abundance patterns, which have been normalized to $\log \varepsilon(\mathrm{Ba}) = 0.0$. The bold black line marks the scaled solar *r*-process pattern, and the thin gray line marks the scaled solar *s*-process pattern (Prantzos et al. 2020). The Pb and Bi abundances in the *s*-process pattern have been enhanced by +1.0 dex relative to the solar pattern to account for the effect of low-metallicity AGB stars (see Figure 20 of Sneden et al. 2008, as calculated in the Appendix of Roederer et al. 2010b). The bottom panel illustrates the differences between the observed abundance patterns and the scaled solar *r*-process pattern.

($Z = 82$) abundances are also signatures of *s*-process enrichment in metal-poor stars (Roederer et al. 2010a), and we do not detect an enhanced Pb abundance in any star in our sample.

The abundance patterns in J1010-0220, J1018-0155, and J1018-0209 are a reasonably close match to the solar *r*-process pattern. The most discrepant element, Y ($Z = 39$), is only discrepant because the solar *r*-process pattern overestimates Y by ≈0.5 dex (e.g., Roederer et al. 2018a). Otherwise, all 11 detected heavy elements lie within $2\sigma$ of the *r*-process pattern in these three stars. Furthermore, the [Ba/Eu] ratio, which is an indicator of the ratio of *r*-process to *s*-process material in a star, is low in these three stars (−0.80, −0.64, and −0.47). Material where the *r*-process is dominant will exhibit [Ba/Eu] $\approx -0.7 \pm 0.2$ (e.g., Sneden et al. 2008; Mashonkina & Christlieb 2014; Prantzos et al. 2020; Roederer et al. 2023), whereas material where the *s*-process is dominant will exhibit [Ba/Eu] $> +1$ (e.g., Sneden et al. 2008; Bisterzo et al. 2014). We conclude that the main component of the *r*-process is the dominant source of the heavy elements in J1010-0220, J1018-0155, and J1018-0209.

Eu ($Z = 63$) is frequently chosen to represent the level of *r*-process enhancement in stars. J1010-0220, J1018-0155, and J1018-0209 are enhanced in *r*-process elements, [Eu/Fe]= $+0.70 \pm 0.21$, $+0.33 \pm 0.15$, and $+0.17 \pm 0.21$, respectively. J1010-0220 and J1018-0155 are therefore members of the *r*-I class of moderately *r*-process-enhanced stars, as defined by Beers & Christlieb (2005) and revised by Holmbeck et al. (2020). This level of enhancement is not as extreme as found in the *r*-process-enhanced UFD galaxy Reticulum II ($+1.0 <$ [Eu/Fe] $< +2.1$; Ji et al. 2016; Roederer et al. 2016), but it is similar to that in the moderately *r*-process-enhanced

UFD galaxy Tucana III ($+0.2 < [Eu/Fe] < +0.6$; Hansen et al. 2017; Marshall et al. 2019). Stars with comparable [Eu/Fe] ratios are found in the Carina,Draco, and Ursa Minor dSph galaxies, although only at higher metallicities ($[Fe/H] > -2.5$; Shetrone et al. 2003; Cohen & Huang 2009, 2010; Venn et al. 2012; Norris et al. 2017).

The other two stars in our sample, J1008+0001 and J1015-0238, exhibit different heavy-element abundance patterns. We discuss J1008+0001 separately in Section 4.5. J1015-0238 has more Sr and less Ba than the other stars in our sample: $\log \varepsilon(Sr/Ba) = 1.90 \pm 0.23$ ($[Sr/Ba] = +1.21 \pm 0.25$), whereas $\log \varepsilon(Sr/Ba) \approx 0.21 \pm 0.18$ ($[Sr/Ba] = -0.48 \pm 0.18$) for the three *r*-process-enhanced stars. The weak component of the *r*-process (e.g., Wanajo 2013) and the weak component of the *s*-process (e.g., Frischknecht et al. 2016) are predicted to be capable of producing enhanced Sr/Ba ratios, and either process could be responsible for the heavy elements in J1015-0238. These processes are associated with core-collapse supernovae or their progenitor stars.

### 4.5. J1008+0001: A CEMP-no Star in Sextans

The star J1008+0001 is located at a projected radius of $10.7\,R_h$ (4.3 kpc) from the center of Sextans, and it is the most widely separated confirmed member of Sextans at present. It is highly enhanced ($[X/Fe] > +1.2$) in the light elements X = C, N, O, Na, Mg, Si, and K. Its [Ca/Fe] ratio, $+0.50 \pm 0.09$, is higher than that found in the other four stars in our sample, $+0.10 \pm 0.05$. It is also highly deficient ($[X/Fe] < -1.4$) in the heavy elements X = Sr and Ba. These characteristics identify J1008+0001 as a member of the class of carbon-enhanced metal-poor stars with no enhancement of neutron-capture elements (CEMP-no; Beers & Christlieb 2005). Such stars are thought to be among the first Population II stars to have formed and among the oldest surviving stars (Norris et al. 2013). No CEMP-no stars have been identified previously in Sextans.

There have been two measurements of $v_{los}$ of this star. One is our measurement ($+223.6 \pm 0.7\,km\,s^{-1}$; Table 2), and the other is an unpublished GIRAFFE measurement obtained on 2019 March 12 as part of a separate program ($+224.4 \pm 5\,km\,s^{-1}$; S. Koposov et al. 2023, in preparation). This star does not exhibit any discernible velocity variations over a span of 3 yr, tentatively suggesting it is not part of a binary or multiple star system.

We fit the light-element abundance pattern (C through Zn; $6 \leqslant Z \leqslant 30$) of J1008+0001 using the yields predicted for zero-metallicity Population III supernovae. We consider theoretical nucleosynthesis yields from the grid of 1D supernova models of Heger & Woosley (2010), which includes nonrotating stars with initial masses ranging from 10–100 $M_\odot$, explosion energies ranging from $0.3 \times 10^{51}$ to $10 \times 10^{51}$ erg, and various degrees of mixing among the ejecta. We construct $10^5$ representations of the observed abundance pattern by resampling the $\log \varepsilon$ abundances from Gaussian distributions with standard deviations given by the observational uncertainties. We find the best-fit model for each resampled abundance pattern using a $\chi^2$ matching algorithm, as described in Placco et al. (2015, 2021a).

Figure 6 illustrates the results of this test. We obtain reasonable fits to most elements. Models with initial masses in the 25–27 $M_\odot$ range are identified as the best fit ≈95% of the time, whereas models with initial masses in the 27–50 $M_\odot$ range are identified ≈5% of the time. No low-mass models are identified as the best fit for any realization. Adopting a N abundance 1 dex lower than the current surface abundance (Section 4.2) does not appreciably change the distribution of best-fit models. Our finding, however, must be interpreted with caution. The chemical evolution models of Hartwig et al. (2018) predict that only metal-poor stars with $[Mg/C] < -1.0$ or so may contain metals produced by a single, dominant progenitor. The [Mg/C] ratio of J1008+0001 is $-0.11 \pm 0.24$, suggesting that it has a low probability of being enriched by a single progenitor. Our results suggest that a massive-star supernova, or perhaps a small number of massive-star supernovae, produced the metals observed today in J1008+0001.

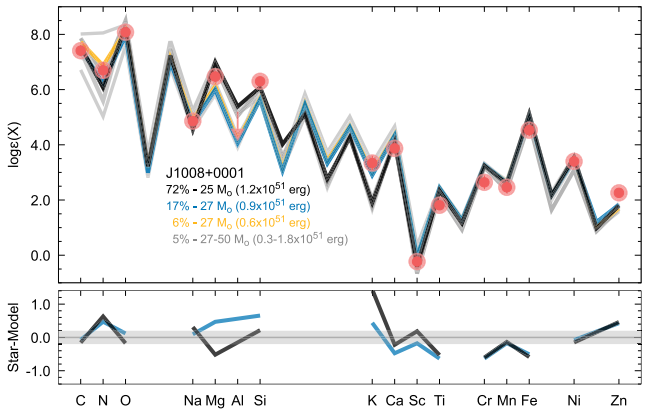


**Figure 6.** Comparison of the abundances in J1008+0001 with yields predicted by zero-metallicity supernova models. The horizontal axis lists the element symbols at their corresponding atomic number ($6 \leqslant Z \leqslant 30$). Top panel: the red dots and downward arrows mark the observed abundance pattern. The lines mark the predicted nucleosynthesis yields, and the colors of these lines correspond to the properties of the progenitor models indicated in the top panel. The percentages next to each model reflect how often that model was selected as the best fit. Bottom panel: the differences between the observed and best-fit patterns are shown for the two models most commonly selected as the best fit. The horizontal gray line marks a difference of 0.0 dex, and the shaded gray band marks ±0.2 dex, an approximate measure of the $1\sigma$ observational uncertainties.

Only two heavy elements are detected in J1008+0001, Sr and Ba. The Sr/Ba ratio in this star, $\log \varepsilon(Sr/Ba) = -0.23 \pm 0.27$ ($[Sr/Ba] = -0.92 \pm 0.32$), is lower than the other stars in our sample, all of which contain more Sr than Ba and exhibit $[Sr/Ba] > -0.55$. These ratios suggest that the Sr and Ba in J1008+0001 could have been synthesized by the weak component of the *s*-process in a rapidly rotating low- or zero-metallicity star. The Frischknecht et al. (2016) weak *s*-process models predict a wide range of potential [Sr/Ba] ratios, depending on the conditions found in each star. These models predict a lower bound in the [Sr/Ba] ratios of ≈ −0.5, which is slightly higher than the ratio in J1008+001. Alternatively, an intermediate neutron-capture process (*i*-process) operating in a low- or zero-metallicity massive ($\sim 25\,M_\odot$) star could also explain the low [Sr/Ba] ratio in J1008+0001 (Banerjee et al. 2018). Either scenario is potentially consistent with the set of zero-metallicity progenitor models inferred from the abundances of lighter elements (Roederer et al. 2014b).

## 5. Discussion

### 5.1. Heavy Elements in Sextans

Multiple heavy-element nucleosynthesis channels were present in the Sextans dwarf galaxy. At least three are apparent among just the five stars in our sample. One is the main

component of the *r*-process, which may occur in neutron-star mergers or exotic massive-star supernovae. The second channel, either the weak component of the *r*-process or the weak component of the *s*-process, accounts for the enhanced Sr/Ba ratio in J1015-0238. The third channel, either the weak component of the *s*-process or the *i*-process, accounts for the deficient Sr/Ba ratio in the CEMP-no star, J1008+0001. These three channels can all be associated with massive-star supernovae or their progenitors. Finally, previous studies (Shetrone et al. 2001; Duggan et al. 2018; Theler et al. 2020) have detected material produced by the main component of the *s*-process in more metal-rich stars ([Fe/H] $> -2.2$) in the inner regions of Sextans, representing a fourth heavy-element synthesis channel. This channel is associated with low- or intermediate-mass AGB stars.

The abundance ratios produced by these channels occupy several distinct regions of chemical space. Three groups of [Ba/Fe] ratios are found in Sextans: one with [Ba/Fe] $\simeq -1$ and $-3.2 <$ [Fe/H] $< -2.3$, one with [Ba/Fe] $\simeq -0.3$ and $-3.0 <$ [Fe/H] $< -2.7$, and one with [Ba/Fe] $\simeq +0.3$ and $-2.5 <$ [Fe/H] $< -1.5$, as shown in Figure 4. We associate them with the weak *r*-process (or weak *s*-process or *i*-process), the main *r*-process, and the *s*-process, respectively.

Our study has expanded the range of heavy-element enrichment processes known to occur in Sextans. Nevertheless, several Sextans stars still lack sufficient chemical information to reliably diagnose the nucleosynthetic origin(s) of their heavy elements. Follow-up observations are warranted to better understand which scenarios occurred in Sextans.

### 5.2. Chemical Inhomogeneity in Sextans

The chemical diversity among the five stars in our sample suggests that stars in the outskirts of Sextans formed in chemically inhomogeneous regions. In contrast, stars in the inner region of Sextans are more chemically homogeneous among the $\alpha$ and *n*-capture elements at a given metallicity (Aoki et al. 2020; Lucchesi et al. 2020; Theler et al. 2020). The Sextans dSph also contrasts with the three UFD galaxies studied by Waller et al. (2023), who found that stars in their outer regions were chemically similar to those near their centers.

Very few CEMP-no stars have been confirmed among stars studied in dSph galaxies: two stars in Carina (Susmitha et al. 2017; Hansen et al. 2023), one star in Draco (Cohen & Huang 2009), two stars in Sculptor (Skúladóttir et al. 2015, 2023), two stars in Ursa Minor (Cohen & Huang 2010), and possibly one star in Canes Venatici (Yoon et al. 2020). The dSph galaxies contrast with the UFD galaxies in this regard because the occurrence frequency of CEMP-no stars in UFD galaxies is relatively high (e.g., Norris et al. 2010; Frebel et al. 2014; Spite et al. 2018; Ji et al. 2020; Chiti et al. 2023). On the other hand, a focused study by Chiti et al. (2018) revealed that the CEMP fraction among stars with [Fe/H] $< -3.0$ in the Sculptor dSph, $36\% \pm 8\%$, is not different from that of the Milky Way halo, $\approx 42\%$. Chiti et al. noted, however, that none of the CEMP stars in their Sculptor sample exhibited [C/Fe] $> +1$. That property is different from the Milky Way halo and UFD galaxies, where stars with [C/Fe] $> +1$ are more common. Skúladóttir et al. (2023) reached a different conclusion from their sample of 11 stars in Sculptor with [Fe/H] $< -3.0$, finding only one CEMP-no star. A fresh analysis may be necessary to resolve this apparent discrepancy in the Sculptor dSph.

Our study is not equipped to derive the CEMP fraction in Sextans. Our results suggest that the outer regions of Sextans, and by extension other more massive dSph galaxies, could be reservoirs of extreme CEMP-no stars. One possible scenario is that these regions may have been similar to those where lower-mass galaxies formed, thereby establishing a common chemical enrichment pathway between galaxies of differing masses. Another possible scenario is that these star-forming regions could have been actual UFD galaxies. This idea is supported by the recent work of Deason et al. (2023), who found that the stellar metallicity distribution of Sextans could allow for the accretion of multiple UFD-like systems. Much larger samples of stars at large radius will be necessary to distinguish among these scenarios.

### 5.3. Substructure in Sextans

Recent observations suggest that extended stellar halos may be a relatively common feature of dwarf galaxies (e.g., Chiti et al. 2021; Stringer et al. 2021; Yang et al. 2022; Sestito et al. 2023b), including Sextans (Qi et al. 2022), even in the absence of tidal distortions. The stars in our sample are located at much larger radii than the stellar substructures in Sextans identified by previous work using stellar velocities and metallicities. We thus cannot directly associate the stars in our sample with that substructure. Future studies of larger samples of stars at large radius will be necessary to potentially associate these chemical signatures with dynamical substructures in Sextans.

## 6. Conclusions

We have collected high-resolution, high-S/N optical spectra of five confirmed member stars of the Sextans dSph galaxy that are located at projected distances of 3.5–10.7 $R_{\rm h}$ (1.4–4.3 kpc) from its center. We identify several chemical signatures absent from previous samples of Sextans stars, including CEMP-no, *r*-process, and enhanced Sr/Ba abundance signatures.

Our results indicate that production of the lighter elements, including $\alpha$, odd-*Z*, and iron-group elements, was dominated by core-collapse supernovae at early times. The mildly enhanced [$\alpha$/Fe] ratios, which are lower in our sample than in typical metal-poor field stars, could indicate a deficiency of metals produced by the highest-mass stars. The outskirts of dSph galaxies, such as Sextans, could represent one birth environment for metal-poor stars occupying the low end of the distribution of [Sc/Fe], [Ti/Fe], and [V/Fe] ratios identified by Cowan et al. (2020). Three stars exhibit moderate enhancement of *r*-process elements. One CEMP-no star exhibits evidence of enrichment dominated by a supernova that produced a chemical signature distinct from that found in the other four stars. All of these chemical signatures can be attributed to enrichment from low-metallicity massive stars, their supernovae, or mergers of neutron stars that result from such supernovae.

We conclude that at least some of the stars in our sample formed in regions with different chemical evolution histories than the stars at the center of Sextans. We anticipate that future studies of stars at large radius in Sextans and other dSph galaxies will reveal a rich diversity of chemical signatures from the first generations of stars and supernovae.

## Acknowledgments

We thank the referee for their helpful comments that have improved this manuscript. We thank the dedicated staff at Las Campanas Observatory for their efforts to develop remote observing capabilities during the COVID-19 travel restrictions. E.O. wishes to remember Jill Bechtold here. We acknowledge generous support from the U.S. National Science Foundation (NSF), provided by grant Nos. AST-1815403 and AST-2205847 (I.U.R., M.M.); AST-1813881, AST-1909584, and AST-2206046 (A.B.P., S.K., M.G.W.); AST-1812461 (N.C.); AST-1815767 (E.W.O.); and PHYS-1430152 (Physics Frontier Center/JINA-CEE; I.U.R.). The work of V.M.P. is supported by NOIRLab, which is managed by AURA under a cooperative agreement with the NSF. This research has made use of NASA's Astrophysics Data System Bibliographic Services; the arXiv preprint server operated by Cornell University; the SIMBAD and VizieR databases hosted by the Strasbourg Astronomical Data Center; the ASD hosted by NIST; and the IRAF software package, which was distributed by the National Optical Astronomy Observatory, which was managed by AURA under a cooperative agreement with the NSF.

*Facilities:* Magellan (MIKE), MMT (Hectochelle), VLT (FLAMES).

*Software:* IRAF (Tody 1993), matplotlib (Hunter 2007), MOOG (Sneden 1973), NumPy (van der Walt et al. 2011), R (R Core Team 2013), SciPy (Virtanen et al. 2020).

## ORCID iDs

Ian U. Roederer https://orcid.org/0000-0001-5107-8930
Andrew B. Pace https://orcid.org/0000-0002-6021-8760
Vinicius M. Placco https://orcid.org/0000-0003-4479-1265
Nelson Caldwell https://orcid.org/0000-0003-2352-3202
Sergey E. Koposov https://orcid.org/0000-0003-2644-135X
Mario Mateo https://orcid.org/0000-0002-3856-232X
Edward W. Olszewski https://orcid.org/0000-0002-7157-500X
Matthew G. Walker https://orcid.org/0000-0003-2496-1925

## References

Abohalima, A., & Frebel, A. 2018, ApJS, 238, 36
Abdurro'uf, Accetta, K., & Aerts, C. 2022, ApJS, 259, 35
Albareti, F. D., Allende Prieto, C., Almeida, A., et al. 2017, ApJS, 233, 25
Amorisco, N. C., Evans, N. W., & van de Ven, G. 2014, Natur, 507, 335
Andrievsky, S. M., Spite, M., Korotin, S. A., et al. 2008, A&A, 481, 481
Aoki, M., Aoki, W., & François, P. 2020, A&A, 636, A111
Aoki, W., Arimoto, N., Sadakane, K., et al. 2009, A&A, 502, 569
Asplund, M., Grevesse, N., Sauval, A. J., & Scott, P. 2009, ARA&A, 47, 481
Banerjee, P., Qian, Y.-Z., & Heger, A. 2018, ApJ, 865, 120
Barklem, P. S., & Aspelund-Johansson, J. 2005, A&A, 435, 373
Barklem, P. S., Piskunov, N., & O'Mara, B. J. 2000, A&A, 355, L5
Battaglia, G., Taibi, S., Thomas, G. F., & Fritz, T. K. 2022, A&A, 657, A54
Battaglia, G., Tolstoy, E., Helmi, A., et al. 2006, A&A, 459, 423
Battaglia, G., Tolstoy, E., Helmi, A., et al. 2011, MNRAS, 411, 1013
Beers, T. C., & Christlieb, N. 2005, ARA&A, 43, 531
Belmonte, M. T., Pickering, J. C., Ruffoni, M. P., et al. 2017, ApJ, 848, 125
Benítez-Llambay, A., Navarro, J. F., Abadi, M. G., et al. 2016, MNRAS, 456, 1185
Bergemann, M., & Cescutti, G. 2010, A&A, 522, A9
Bergemann, M., & Gehren, T. 2008, A&A, 492, 823
Bergemann, M., Lind, K., Collet, R., Magic, Z., & Asplund, M. 2012, MNRAS, 427, 27
Bergemann, M., Pickering, J. C., & Gehren, T. 2010, MNRAS, 401, 1334
Bernstein, R., Shectman, S. A., Gunnels, S. M., Mochnacki, S., & Athey, A. E. 2003, Proc. SPIE, 4841, 1694
Bettinelli, M., Hidalgo, S. L., Cassisi, S., Aparicio, A., & Piotto, G. 2018, MNRAS, 476, 71
Biémont, E., Garnir, H. P., Palmeri, P., Li, Z. S., & Svanberg, S. 2000, MNRAS, 312, 116
Biémont, É. 2011, MNRAS, 414, 3350
Bisterzo, S., Travaglio, C., Gallino, R., Wiescher, M., & Käppeler, F. 2014, ApJ, 787, 10
Blackwell, D. E., Petford, A. D., Shallis, M. J., & Simmons, G. J. 1982, MNRAS, 199, 43
Bohlin, R. C., Savage, B. D., & Drake, J. F. 1978, ApJ, 224, 132
Brown, A. G. A., Vallenari, A., Prusti, T., et al. 2021, A&A, 649, A1
Brown, T. M., Tumlinson, J., Geha, M., et al. 2014, ApJ, 796, 91
Casagrande, L., & VandenBerg, D. A. 2014, MNRAS, 444, 392
Castelli, F., & Kurucz, R. L. 2003, in IAU Symp. 210, Modelling of Stellar Atmospheres, ed. N. Piskunov, W. W. Weiss, & D. F. Gray (Cambridge: Cambridge Univ. Press)
Cayrel, R., Depagne, E., Spite, M., et al. 2004, A&A, 416, 1117
Chiti, A., Frebel, A., Ji, A. P., et al. 2023, AJ, 165, 55
Chiti, A., Frebel, A., Simon, J. D., et al. 2021, NatAs, 5, 392
Chiti, A., Simon, J. D., Frebel, A., et al. 2018, ApJ, 856, 142
Cicuéndez, L., & Battaglia, G. 2018, MNRAS, 480, 251
Cicuéndez, L., Battaglia, G., Irwin, M., et al. 2018, A&A, 609, A53
Cohen, J. G., & Huang, W. 2009, ApJ, 701, 1053
Cohen, J. G., & Huang, W. 2010, ApJ, 719, 931
Cowan, J. J., Sneden, C., Roederer, I. U., et al. 2020, ApJ, 890, 119
Deason, A. J., Koposov, S. E., Fattahi, A., & Grand, R. J. J. 2023, MNRAS, 520, 6091
Den Hartog, E. A., Lawler, J. E., Sneden, C., et al. 2021, ApJS, 255, 27
Den Hartog, E. A., Lawler, J. E., Sneden, C., Cowan, J. J., & Brukhovesky, A. 2019, ApJS, 243, 33
Den Hartog, E. A., Lawler, J. E., Sneden, C., Roederer, I. U., & Cowan, J. J. 2023, ApJS, 265, 42
Den Hartog, E. A., Lawler, J. E., Sneden, C., & Cowan, J. J. 2003, ApJS, 148, 543
Den Hartog, E. A., Lawler, J. E., Sobeck, J. S., Sneden, C., & Cowan, J. J. 2011, ApJS, 194, 35
Den Hartog, E. A., Ruffoni, M. P., Lawler, J. E., et al. 2014, ApJS, 215, 23
Dey, A., Schlegel, D. J., Lang, D., et al. 2019, AJ, 157, 168
Duggan, G. E., Kirby, E. N., Andrievsky, S. M., & Korotin, S. A. 2018, ApJ, 869, 50
Ferlet, R., Vidal-Madjar, A., & Gry, C. 1985, ApJ, 298, 838
Fernandes, L., Mason, A. C., Horta, D., et al. 2023, MNRAS, 519, 3611
Filion, C., & Wyse, R. F. G. 2021, ApJ, 923, 218
Frebel, A., Casey, A. R., Jacobson, H. R., & Yu, Q. 2013, ApJ, 769, 57
Frebel, A., Kirby, E. N., & Simon, J. D. 2010, Natur, 464, 72
Frebel, A., & Norris, J. E. 2015, ARA&A, 53, 631
Frebel, A., Simon, J. D., & Kirby, E. N. 2014, ApJ, 786, 74
Frischknecht, U., Hirschi, R., Pignatari, M., et al. 2016, MNRAS, 456, 1803
Fritz, T. K., Battaglia, G., Pawlowski, M. S., et al. 2018, A&A, 619, A103
Fulbright, J. P., Rich, R. M., & Castro, S. 2004, ApJ, 612, 447
Griffen, B. F., Dooley, G. A., Ji, A. P., et al. 2018, MNRAS, 474, 443
Hansen, T. T., Simon, J. D., Li, T. S., et al. 2023, A&A, 674, A180
Hansen, T. T., Simon, J. D., Marshall, J. L., et al. 2017, ApJ, 838, 44
Hartwig, T., Yoshida, N., Magg, M., et al. 2018, MNRAS, 478, 1795
Heger, A., & Woosley, S. E. 2010, ApJ, 724, 341
Helmi, A., van Leeuwen, F., McMillan, P. J., et al. 2018, A&A, 616, A12
Hendricks, B., Koch, A., Walker, M., et al. 2014, A&A, 572, A82
Holmbeck, E. M., Hansen, T. T., Beers, T. C., et al. 2020, ApJS, 249, 30
Honda, S., Aoki, W., Arimoto, N., & Sadakane, K. 2011, PASJ, 63, 523
Hunter, J. D. 2007, CSE, 9, 90
Ivans, I. I., Simmerer, J., Sneden, C., et al. 2006, ApJ, 645, 613
Ji, A. P., Frebel, A., Simon, J. D., & Chiti, A. 2016, ApJ, 830, 93
Ji, A. P., Li, T. S., Simon, J. D., et al. 2020, ApJ, 889, 27
Jofré, P., Heiter, U., & Soubiran, C. 2019, ARA&A, 57, 571
Jordi, K., Grebel, E. K., & Ammon, K. 2006, A&A, 460, 339
Kelson, D. D. 2003, PASP, 115, 688
Kelson, D. D., Illingworth, G. D., van Dokkum, P. G., & Franx, M. 2000, ApJ, 531, 159
Kim, H.-S., Han, S.-I., Joo, S.-J., Jeong, H., & Yoon, S.-J. 2019, ApJL, 870, L8
Kirby, E. N., Cohen, J. G., Smith, G. H., et al. 2011a, ApJ, 727, 79
Kirby, E. N., Lanfranchi, G. A., Simon, J. D., Cohen, J. G., & Guhathakurta, P. 2011b, ApJ, 727, 78
Kleyna, J. T., Wilkinson, M. I., Evans, N. W., & Gilmore, G. 2004, MNRAS, 354, L66
Kramida, A., Ralchenko, Y., Reader, J. & NIST ASD Team 2021, NIST Atomic Spectra Database (v5.9), [online], https://physics.nist.gov/asd
Kurucz, R. L. 2011, CaJPh, 89, 417
Lai, D. K., Bolte, M., Johnson, J. A., et al. 2008, ApJ, 681, 1524
Lawler, J. E., Bonvallet, G., & Sneden, C. 2001a, ApJ, 556, 452

Lawler, J. E., Wickliffe, M. E., den Hartog, E. A., & Sneden, C. 2001b, ApJ, 563, 1075
Lawler, J. E., & Dakin, J. T. 1989, JOSAB, 6, 1457
Lawler, J. E., Den Hartog, E. A., Sneden, C., & Cowan, J. J. 2006, ApJS, 162, 227
Lawler, J. E., Guzman, A., Wood, M. P., Sneden, C., & Cowan, J. J. 2013, ApJS, 205, 11
Lawler, J. E., Sneden, C., & Cowan, J. J. 2015, ApJS, 220, 13
Lawler, J. E., Sneden, C., Cowan, J. J., Ivans, I. I., & Den Hartog, E. A. 2009, ApJS, 182, 51
Lawler, J. E., Sneden, C., Nave, G., et al. 2017, ApJS, 228, 10
Lawler, J. E., Wood, M. P., Den Hartog, E. A., et al. 2014, ApJS, 215, 20
Li, R., Chatelain, R., Holt, R. A., et al. 2007, PhyS, 76, 577
Lind, K., Asplund, M., & Barklem, P. S. 2009, A&A, 503, 541
Lind, K., Asplund, M., Barklem, P. S., & Belyaev, A. K. 2011, A&A, 528, A103
Lind, K., Bergemann, M., & Asplund, M. 2012, MNRAS, 427, 50
Ljung, G., Nilsson, H., Asplund, M., & Johansson, S. 2006, A&A, 456, 1181
Longeard, N., Jablonka, P., Arentsen, A., et al. 2022, MNRAS, 516, 2348
Longeard, N., Jablonka, P., Battaglia, G., et al. 2023, arXiv:2304.13046
Lucchesi, R., Lardo, C., Primas, F., et al. 2020, A&A, 644, A75
Marshall, J. L., Hansen, T., Simon, J. D., et al. 2019, ApJ, 882, 177
Mashonkina, L., & Christlieb, N. 2014, A&A, 565, A123
Mashonkina, L., Jablonka, P., Sitnova, T., Pakhomov, Y., & North, P. 2017, A&A, 608, A89
Mashonkina, L., Pakhomov, Y. V., Sitnova, T., et al. 2022, MNRAS, 509, 3626
Mashonkina, L., Ryabtsev, A., & Frebel, A. 2012, A&A, 540, A98
Masseron, T., Plez, B., Van Eck, S., et al. 2014, A&A, 571, A47
McWilliam, A. 1998, AJ, 115, 1640
McWilliam, A., Wallerstein, G., & Mottini, M. 2013, ApJ, 778, 149
Meléndez, J., & Barbuy, B. 2009, A&A, 497, 611
Muñoz, R. R., Côté, P., Santana, F. A., et al. 2018, ApJ, 860, 66
Muñoz, R. R., Frinchaboy, P. M., Majewski, S. R., et al. 2005, ApJL, 631, L137
Muñoz, R. R., Majewski, S. R., Zaggia, S., et al. 2006, ApJ, 649, 201
Nordlander, T., & Lind, K. 2017, A&A, 607, A75
Norris, J. E., Yong, D., Venn, K. A., et al. 2017, ApJS, 230, 28
Norris, J. E., Gilmore, G., Wyse, R. F. G., Yong, D., & Frebel, A. 2010, ApJL, 722, L104
Norris, J. E., Yong, D., Bessell, M. S., et al. 2013, ApJ, 762, 28
O'Brian, T. R., Wickliffe, M. E., Lawler, J. E., Whaling, W., & Brault, J. W. 1991, JOSAB, 8, 1185
Olszewski, E. W., & Aaronson, M. 1985, AJ, 90, 2221
Olszewski, E. W., Mateo, M., Harris, J., et al. 2006, AJ, 131, 912
Osorio, Y., & Barklem, P. S. 2016, A&A, 586, A120
Osorio, Y., Barklem, P. S., Lind, K., et al. 2015, A&A, 579, A53
Ou, X., Roederer, I. U., Sneden, C., et al. 2020, ApJ, 900, 106
Pace, A. B., Erkal, D., & Li, T. S. 2022, ApJ, 940, 136
Pace, A. B., Kaplinghat, M., Kirby, E., et al. 2020, MNRAS, 495, 3022
Pakhomov, Y. V., Ryabchikova, T. A., & Piskunov, N. E. 2019, ARep, 63, 1010
Pasquini, L., Avila, G., Blecha, A., et al. 2002, Msngr, 110, 1
Pehlivan Rhodin, A., Hartman, H., Nilsson, H., & Jönsson, P. 2017, A&A, 598, A102
Pickering, J. C., Thorne, A. P., & Perez, R. 2001, ApJS, 132, 403
Pickering, J. C., Thorne, A. P., & Perez, R. 2002, ApJS, 138, 247
Piskunov, N. E., Kupka, F., Ryabchikova, T. A., Weiss, W. W., & Jeffery, C. S. 1995, A&AS, 112, 525
Placco, V. M., Frebel, A., Beers, T. C., & Stancliffe, R. J. 2014, ApJ, 797, 21
Placco, V. M., Frebel, A., Lee, Y. S., et al. 2015, ApJ, 809, 136
Placco, V. M., Sneden, C., Roederer, I. U., et al. 2021b, RNAAS, 5, 92
Placco, V. M., Roederer, I. U., Lee, Y. S., et al. 2021a, ApJL, 912, L32
Prantzos, N., Abia, C., Cristallo, S., Limongi, M., & Chieffi, A. 2020, MNRAS, 491, 1832
Prusti, T., de Bruijne, J. H. J. & (Gaia Collaboration) 2016, A&A, 595, A1
Qi, Y., Zivick, P., Pace, A. B., Riley, A. H., & Strigari, L. E. 2022, MNRAS, 512, 5601
R Core Team 2013, Language and Environment for Statistical Computing, R Foundation for Statistical Computing, http://www.R-project.org
Reichert, M., Hansen, C. J., Hanke, M., et al. 2020, A&A, 641, A127
Revaz, Y., Jablonka, P., Sawala, T., et al. 2009, A&A, 501, 189
Rey, M. P., Pontzen, A., Agertz, O., et al. 2019, ApJL, 886, L3
Roderick, T. A., Jerjen, H., Da Costa, G. S., & Mackey, A. D. 2016, MNRAS, 460, 30
Roederer, I. U., Cowan, J. J., Karakas, A. I., et al. 2010a, ApJ, 724, 975
Roederer, I. U., Sneden, C., Thompson, I. B., Preston, G. W., & Shectman, S. A. 2010b, ApJ, 711, 573
Roederer, I. U., & Lawler, J. E. 2012, ApJ, 750, 76
Roederer, I. U., & Lawler, J. E. 2021, ApJ, 912, 119
Roederer, I. U., Lawler, J. E., Sneden, C., et al. 2008, ApJ, 675, 723
Roederer, I. U., Lawler, J. E., Sobeck, J. S., et al. 2012, ApJS, 203, 27
Roederer, I. U., Mateo, M., Bailey, J. I., III, et al. 2016, AJ, 151, 82
Roederer, I. U., Preston, G. W., Thompson, I. B., et al. 2014a, AJ, 147, 136
Roederer, I. U., Preston, G. W., Thompson, I. B., Shectman, S. A., & Sneden, C. 2014b, ApJ, 784, 158
Roederer, I. U., Sakari, C. M., Placco, V. M., et al. 2018a, ApJ, 865, 129
Roederer, I. U., Sneden, C., Lawler, J. E., et al. 2018b, ApJ, 860, 125
Roederer, I. U., Vassh, N., Holmbeck, E. M., et al. 2023, Sci, submitted.
Ruffoni, M. P., Den Hartog, E. A., Lawler, J. E., et al. 2014, MNRAS, 441, 3127
Saha, M. N. 1921, RSPSA, 99, 135
Sbordone, L., Bonifacio, P., Caffau, E., et al. 2010, A&A, 522, A26
Schlafly, E. F., & Finkbeiner, D. P. 2011, ApJ, 737, 103
Sestito, F., Roediger, J., Navarro, J. F., et al. 2023a, MNRAS, 523, 123
Sestito, F., Zaremba, D., Venn, K. A., et al. 2023b, arXiv:2301.13214
Shetrone, M. D., Côté, P., & Sargent, W. L. W. 2001, ApJ, 548, 592
Shetrone, M., Venn, K. A., Tolstoy, E., et al. 2003, AJ, 125, 684
Shi, J. R., Gehren, T., Mashonkina, L., & Zhao, G. 2009, A&A, 503, 533
Sitnova, T. M., Mashonkina, L. I., & Ryabchikova, T. A. 2016, MNRAS, 461, 1000
Skúladóttir, Á., Tolstoy, E., Salvadori, S., et al. 2015, A&A, 574, A129
Skúladóttir, Á., Vanni, I., Salvadori, S., & Lucchesi, R. 2023, arXiv:2305.02829
Smith, V. V., Lambert, D. L., & Nissen, P. E. 1998, ApJ, 506, 405
Sneden, C., Boesgaard, A. M., Cowan, J. J., et al. 2023, ApJ, 953, 31
Sneden, C., Cowan, J. J., & Gallino, R. 2008, ARA&A, 46, 241
Sneden, C., Lawler, J. E., Cowan, J. J., Ivans, I. I., & Den Hartog, E. A. 2009, ApJS, 182, 80
Sneden, C., Lucatello, S., Ram, R. S., Brooke, J. S. A., & Bernath, P. 2014, ApJS, 214, 26
Sneden, C. A. 1973, PhD thesis, The University of Texas at Austin
Sobeck, J. S., Kraft, R. P., Sneden, C., et al. 2011, AJ, 141, 175
Sobeck, J. S., Lawler, J. E., & Sneden, C. 2007, ApJ, 667, 1267
Spite, F., & Spite, M. 1982, A&A, 115, 357
Spite, M., Spite, F., François, P., et al. 2018, A&A, 617, A56
Spitzer, L. 1978, Physical Processes in the Interstellar Medium (New York: Wiley)
Starkenburg, E., Hill, V., Tolstoy, E., et al. 2010, A&A, 513, A34
Stringer, K. M., Drlica-Wagner, A., Macri, L., et al. 2021, ApJ, 911, 109
Susmitha, A., Koch, A., & Sivarani, T. 2017, A&A, 606, A112
Szentgyorgyi, A., Furesz, G., Cheimets, P., et al. 2011, PASP, 123, 1188
Tafelmeyer, M., Jablonka, P., Hill, V., et al. 2010, A&A, 524, A58
Takeda, Y., Zhao, G., Chen, Y.-Q., Qiu, H.-M., & Takada-Hidai, M. 2002, PASJ, 54, 275
Tarumi, Y., Yoshida, N., & Frebel, A. 2021, ApJL, 914, L10
Theler, R., Jablonka, P., Lucchesi, R., et al. 2020, A&A, 642, A176
Thévenin, F., & Idiart, T. P. 1999, ApJ, 521, 753
Tody, D. 1993, in ASP Conf. Ser. 52, Astronomical Data Analysis Software and Systems II, ed. R. J. Hanisch, R. J. V. Brissenden, & J. Barnes (San Francisco, CA: ASP), 173
Tokiwa, A., Takada, M., Qiu, T., et al. 2023, arXiv:2302.06071
Unsöld, A. 1955, Physik der Sternatmospharen, MIT besonderer Berucksichtigung der Sonne (Berlin: Springer)
van der Walt, S., Colbert, S. C., & Varoquaux, G. 2011, CSE, 13, 22
Venn, K. A., Shetrone, M. D., Irwin, M. J., et al. 2012, ApJ, 751, 102
Virtanen, P., Gommers, R., Oliphant, T. E., et al. 2020, NatMe, 17, 261
Walker, M. G., Mateo, M., Olszewski, E. W., et al. 2006, ApJL, 642, L41
Walker, M. G., Mateo, M., & Olszewski, E. W. 2009a, AJ, 137, 3100
Walker, M. G., Mateo, M., Olszewski, E. W., Sen, B., & Woodroofe, M. 2009b, AJ, 137, 3109
Waller, F., Venn, K. A., Sestito, F., et al. 2023, MNRAS, 519, 1349
Wanajo, S. 2013, ApJL, 770, L22
Weisz, D. R., Dolphin, A. E., Skillman, E. D., et al. 2014, ApJ, 789, 147
Westfall, K. B., Majewski, S. R., Ostheimer, J. C., et al. 2006, AJ, 131, 375
Wickliffe, M. E., Lawler, J. E., & Nave, G. 2000, JQSRT, 66, 363
Wood, M. P., Lawler, J. E., Den Hartog, E. A., Sneden, C., & Cowan, J. J. 2014a, ApJS, 214, 18
Wood, M. P., Lawler, J. E., Sneden, C., & Cowan, J. J. 2014b, ApJS, 211, 20
Wood, M. P., Lawler, J. E., Sneden, C., & Cowan, J. J. 2013, ApJS, 208, 27
Yang, Y., Hammer, F., Jiao, Y., & Pawlowski, M. S. 2022, MNRAS, 512, 4171
Yong, D., Norris, J. E., Bessell, M. S., et al. 2013, ApJ, 762, 26
Yoon, J., Whitten, D. D., Beers, T. C., et al. 2020, ApJ, 894, 7